PhD thesis

Title

Towards a numerical derivation of maximal Kerr trumpet initial data

Author

Gernot Heißel, BSc, MSc

Aspired degree

Doctor of Philosophy (PhD)

Cardiff, 2017

Thesis adviser	Prof Mark Hannam
Second adviser	Prof Stephen Fairhurst

Ganz wesentlich scheint dabei die Fähigkeit, das Gleichgewicht wiederzufinden, denn es gibt sehr verschiedene Arten des Zweifels. Es gibt den alles zersetzenden Zweifel, der jede sich anbietende Wirklichkeit nur zerstören will und der schließlich in die Ver-Zweiflung führt, weil sich nirgends mehr fester Halt findet. Und es gibt den Zweifel, der der Einsicht in die wundersame Struktur der Wirklichkeit entspringt, der danach trachtet, bloße Wunschvorstellungen und Hoffnungen als solche zu erkennen und gerade dadurch festen Boden zu gewinnen. Es ist diese Art des Zweifels, die uns die einzige Möglichkeit bietet, unsere eigene Wirklichkeit vor der Realität nicht ganz zu entfernen.

Herbert Pietschmann – Die Wahrheit liegt nicht in der Mitte

Acknowledgements

First and foremost, I thank my thesis adviser Prof Mark Hannam for many helpful discussions in regular and frequent meetings and for often pointing me in the right direction in my research with his advice. Thanks also to my second adviser Prof Stephen Fairhurst, in particular for his useful advise in the regular progress report meetings. The same holds for my mentor Dr David I Westwood.

Many thanks also to my parents, Reinhild and Gunther, for their incredible support during my time here in Cardiff, including helping me to move here, visiting me in summer and welcoming me back home when I came for visit. They always supported me in my education and in pursuing my goals, throughout my life really.

A big thank you to my girlfriend Chen, who balanced my work-life, while at the same time showing a lot of support for my work on the thesis, especially during the writeup phase. As much as I enjoyed my research, I was always looking forward to her next visit, or me visiting her for the next time.

I also wish to thank my friends back in Austria, all of them really, but in particular Beni and Piwo for always spending time with me when I was back home, and for hanging out with me in the depth of the internet when I was not. Also thanks to Beni, Piwo and Reb, for visiting me in Cardiff to celebrate my 30th birthday.

A great thank you also to my colleagues and friends here in Cardiff, for at least part of my time here – all of them really, but in particular Max and Valeriu for often cheering me up with their temperament, for persuading me to go for 'brewskis' and for many good conversations, both the more intellectual ones, and the less intellectual, but nonetheless not less valuable ones. The same, minus the 'brewskis', holds for Seb, Alex and many others – you know who you are.

I do not have the slightest ideas about all the administrative work related to having me as PhD student in the school, but I would like to thank Louise Winter representatively. She was always a great help and fast and precise in reply when I had a question.

Last but not least, thanks to the Science and Technology Facilities Council for funding my research.

Thank you!

Contents

CHAPTER 1

Introduction

It is now roughly a century ago since Einstein developed his his theory of space, time and gravitation – general relativity – in 1915. While many of its weak field predictions could soon be tested, and have since been tested with ever increasing accuracy, up until recently there have been little experimental insights into the strong field regime of the theory. Notably, there has been the indirect verification of gravitational waves radiating from the Hulse-Taylor pulsar binary by observing the reduction of its rotation period over time. But it took until 2015 when gravitational waves could first be detected directly, on our soil, using laser interferometers. Why did it take one hundred years? The challenges were huge on many fronts. On the one hand there is the enormous challenge to engineer interferometers which are sensitive enough to measure such tiny changes in the length of their arms caused by fly-by gravitational waves. But even with high enough accuracy, the gravitational wave signals are still buried deep in the detector noise, which imposes a huge challenge on the data analysis. One technique to deal with that is to comb the data with filters, which match the gravitational wave signals. In order to apply this technique, the waveforms have to be provided by the theory, ie by general relativity, or in practice, by waveform models which are gauged against the theory.

The strongest sources of gravitational waves are black hole binaries in mutual orbit, which spiral in and ultimately merge as a result of their decreasing separation due to the gravitational wave emission. The task to accurately calculate the waveforms extracted from these systems in the full theory of relativity was another major challenge, and required enormous advances in the field of numerical relativity. Only in 2005 did long term simulations become possible, covering the in-spiral, merger and ring-down for the first time. Two approaches yielded success, which differ in the way in which they avoid to have to deal with the black hole singularities numerically. One of them excises a region around the singularities by engineering from the numerical domain – the excision method. The other works in a gauge in which the singularities are not on the numerical domain in the first place – the moving puncture method.

Even though the binary black hole problem is now essentially solved, progress has since been made in optimising the approaches. With this thesis we hope to contribute to the improvement of the initial data formalism. In the moving puncture approach, black holes are initially modeled via a wormhole geometry, which avoids the singularity via its throat, bridging two asymptotically flat ends. However it has been shown that the wormholes change their geometry, and asymptote to what has been called trumpets during the evolution. A trumpet is still a singularity avoiding representation of a black hole. It however lacks the second asymptotically flat end of a wormhole, and instead connects the physical flat end to a throat of finite area, where it terminates. Initial data in this form has since been constructed for Schwarzschild and other black hole spacetimes, such as Bowen-York. The problem to construct such initial data for Kerr spacetime, in a form which is suited for numerical evolution code, however remains still open.

In this thesis we work towards a numerical derivation of Kerr trumpet initial data in maximal gauge. In part 1 we summarise the necessary theoretical background as well as the relevant literature on trumpet initial data, and we lay out the numerical methods which we use in part 2 to solve the initial data equations. In part 2 we then present the novel research of this thesis. We outline the proposed approach, and present our main results: the test of the approach in the special cases of zero and maximal spin – ie for Schwarzschild and extreme Kerr spacetime. The work of this thesis constitutes the first numerical construction of trumpet data for these key examples, and lays the foundation for the construction of general trumpet black-hole data in the future.

Part 1

Background

CHAPTER 2

The initial data formalism in $3+1$ numerical relativity

The goal of this chapter is to arrive at the $3+1$ initial data formalism in weighted transverse decomposition and in conformal thin sandwich decomposition. These provide the formal theoretical setting for the analyses in part 2. In section 1 we summarise general relativity in its original four-dimensional formulation. After we perform a $3+1$ split of spacetime in section 2, we then formulate the theory as initial data problem in section 3. Finally, we develop the initial data formalism in the weighted transverse decomposition in section 4, and relate it to the conformal thin sandwich decomposition in section 5. For thorough standard text books on the material presented here we refer to [1, 8].

Greek indices $\{\mu, \nu, \dots\}$ refer to components of spacetime quantities, and latin indices $\{i, j, \dots\}$ denote components of spatial quantities. Component matrices are denoted by brackets, ie $[g_{\mu\nu}]$. We denote $K = \operatorname{tr} K$ for the trace of the extrinsic curvature and other quantities, however we use $\gamma = \det \gamma$ for the determinant of the spatial, and other metrics.

1. General relativity

Einstein's theory of general relativity spacetime is modeled as a four-dimensional semi-Riemannian manifold with signature $(-+++)$. Gravitation enters by requiring the spacetime's metric $g_{\mu\nu}$ to satisfy the Einstein equation,

Einstein equation

$$\tilde{R}_{\mu\nu} - \frac{\tilde{R}}{2} g_{\mu\nu} = 8\pi T_{\mu\nu}, \tag{1}$$

where $\tilde{R}_{\mu\nu}$ and $\tilde{R}$ denote the Ricci tensor and Ricci scalar associated with the spacetime metric; cf standard textbooks such as [46, 29, 34, 48]. $T_{\mu\nu}$ denotes the stress-energy tensor associated with the spacetime metric and the matter content. Thus, the Einstein equation (1) relates a measure of spacetime geometry, specifically of intrinsic curvature, to a measure of matter-energy density.

Einstein's theory marked a paradigm shift of the way in which we think about space, time and gravitation. These aspects of the theory are inherent in the four-dimensional formulation. However, at the same time, this formulation has its practical limits when it comes to the construction of astrophysically relevant solutions which lack a sufficiently high degree of symmetry, such as solutions to the binary black hole problem. For these problems it is more natural, and turned out to be more successful, to think in terms of a gravitational field in three-dimensional space that evolves in time – a dynamic description that is obscured in the static picture of the original, four-dimensional formulation.

2. The 3+1 split of spacetime

A particularly successful approach is the $3+1$ formulation of general relativity where one views a spacetime M as being chopped up into spatial hypersurfaces Σ_t, called slices; cf [4, 49] or [1, 8]. A one-parameter family $\{\Sigma_t\}$, with $M = \bigcup_t \Sigma_t$, is called a foliation of M. Obviously a foliation is not unique to a spacetime, as illustrated in figure 1. There are infinite ways to foliate it.

slices and foliations

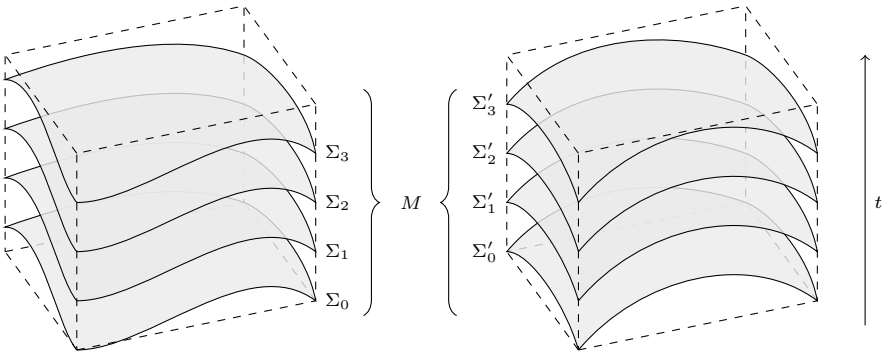

FIGURE 1. The three-dimensional spatial slices Σ_t and Σ'_t both foliate the spacetime M. One space dimension is suppressed for representability.

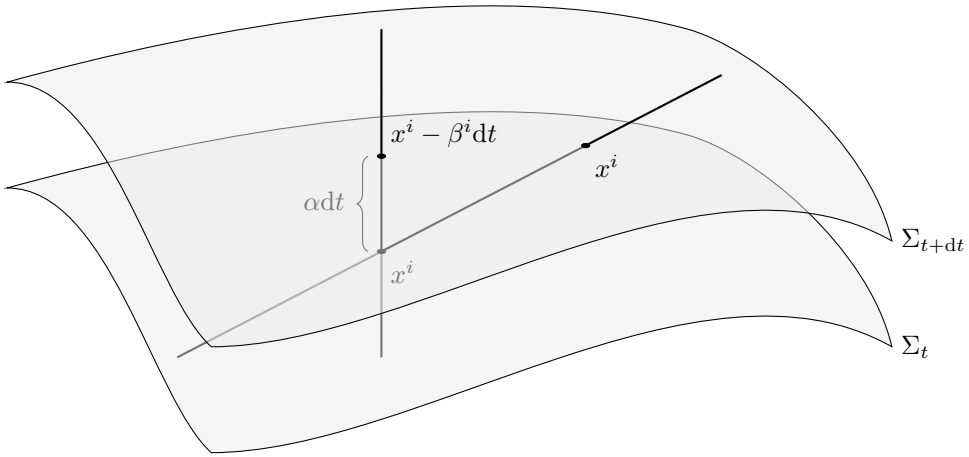

FIGURE 2. Interpretation of the gauge functions: α describes the time lapse, and β^i the spatial shift of the coordinates x^i between two neighbouring slices.

Let now $\{\Sigma_t\}$ be a foliation of spacetime. It is convenient to choose spatial basis vectors that are tangent to the slices. The components of the spacetime metric $g_{\mu\nu}$ and it's inverse $g^{\mu\nu}$ can then be written as

$$[g_{\mu\nu}] = \begin{bmatrix} -\alpha^2 + \beta_k\beta^k & \beta_i \\ \beta_j & \gamma_{ij} \end{bmatrix} \quad \text{and} \quad [g^{\mu\nu}] = \begin{bmatrix} -1/\alpha^2 & \beta^i/\alpha^2 \\ \beta^j/\alpha^2 & \gamma^{ij} - \beta^i\beta^j/\alpha^2 \end{bmatrix}, \tag{2}$$

and the basis expansion of the metric, ie the line element, is given as

$$\mathrm{d}s^2 = (-\alpha^2 + \beta_i\beta^i)\mathrm{d}t^2 + 2\beta_i \mathrm{d}t\mathrm{d}x^i + \gamma_{ij}\mathrm{d}x^i\mathrm{d}x^j.$$

spatial metric, gauge functions

This does not pose a restriction on the metric – any metric can be written in this way. γ_{ij} denotes the spatial metric on the slices. α specifies the time-lapse between a slice Σ_t and a neighbouring slice $\Sigma_{t+\mathrm{d}t}$ along the line normal to the slices, and is called the lapse function. β^i on the other hand specifies the shift that the spatial coordinates x^i undergo with respect to the line normal to the slices, between time t and $t + \mathrm{d}t$. It is called the shift vector. Together α and β^i are referred to as the gauge functions; cf figure 2. From (2) we see that instead of describing the gravitational field as a four-dimensional metric $g_{\mu\nu}$ on spacetime M, we can as well

describe it as a three-dimensional metric γ_{ij} together with a set of gauge functions $\{\alpha, \beta^i\}$ on each slice of a foliation $\{\Sigma_t\}$ of M. This can be seen as a 3+1 description of the gravitational field.

The standard $3+1$ formalism however goes one step further and introduces the extrinsic curvature K_{ij} on the slices. It can be defined as the Lie-derivative of the spatial metric along the vector normal to the slices, up to a factor $-1/2$. Expressed in a foliation adapted frame, this becomes

extrinsic curvature

$$K_{ij} = -\frac{1}{2\alpha}(\partial_t \gamma_{ij} - D_i\beta_j - D_j\beta_i); \tag{3}$$

cf [1, p 70, 71]. D_i denotes the covariant derivative with respect to γ_{ij} on the slices, and since indices of spacial tensors are being pulled by the spatial metric we have $\beta_i = \gamma_{ik}\beta^k$. The $3+1$ formulation then views the set $\{\gamma_{ij}, K_{ij}\}$ on each slice of a foliation $\{\Sigma_t\}$ as the fundamental variables describing the gravitational field, which is again equivalent to providing the spacetime metric $g_{\mu\nu}$ on M.

3. The 3+1 formulation of general relativity

So far we have encountered three ways to describe the gravitational field in spacetime, which we shall symbolically summarise by

$$g_{\mu\nu} \text{ on } M \quad \longleftrightarrow \quad \{\gamma_{ij}, \alpha, \beta^i\} \text{ on } \{\Sigma_t\} \quad \longleftrightarrow \quad \{\gamma_{ij}, K_{ij}\} \text{ on } \{\Sigma_t\}.$$

The former provides a four-dimensional description, while the latter two are $3+1$ descriptions. The standard 3+1 formulation works with the quantities $\{\gamma_{ij}, K_{ij}\}$, ie with the spatial metric and extrinsic curvature. What is left to do is to formulate the laws of gravitation, ie the Einstein equation (1), in a $3+1$ form for these variables.

The idea is to first prescribe the gravitational field $\{\gamma_{ij}, K_{ij}\}$ on an initial slice Σ_0 and to then evolve these quantities in time to obtain the field for all times, ie on the foliation $\{\Sigma_t\}$. This means that the $3+1$ Einstein equations have to be split up in a set of constraint and time evolution equations. While the constraint equations will ensure that the gravitational field $\{\gamma_{ij}, K_{ij}\}$ satisfies the laws of gravitation on the initial slice Σ_0, the time evolution equations will ensure that this field also evolves in time, ie from slice to slice, according to the laws of gravitation. The latter also implies that the constraints will continue to be satisfied on all future slices.

One of these equations, the time evolution equation for the metric, is readily given by (3), which becomes clear if we rewrite it as

evolution equations

$$\partial_t \gamma_{ij} = -2\alpha K_{ij} + D_i\beta_j + D_j\beta_i. \tag{4}$$

To find the remaining equations, one has to consider various projections of the spacetime Riemann tensor $\tilde{R}^{\mu}{}_{\nu\rho\sigma}$ associated with $g_{\mu\nu}$ onto the slices Σ_t and onto the vector normal to the slices. This way $\tilde{R}^{\mu}{}_{\nu\rho\sigma}$ can be expressed in terms of the spatial Riemann tensor $R^i{}_{jkl}$ associated with γ_{ij} and the extrinsic curvature K_{ij} on the slices. Using then the Einstein equation (1) in the right places to relate the geometric quantities to the matter sources, one obtains two additional constraint equations (four in components), and an evolution equation for the extrinsic curvature K_{ij}; cf [1, section 2.4, 2.5] or [8, section 2.5, 2.6, 2.7]. The latter is given by

$$\begin{aligned} \partial_t K_{ij} = {} & \alpha(R_{ij} - 2K_{ik}K^k{}_j + K_{ij}) - D_iD_j\alpha \\ & - 8\pi\alpha\Big(S_{ij} - \frac{1}{2}\gamma_{ij}(S-\rho)\Big) + \beta^k\partial_k K_{ij} + K_{ik}\partial_j\beta^k + K_{kj}\partial_i\beta^k. \end{aligned} \tag{5}$$

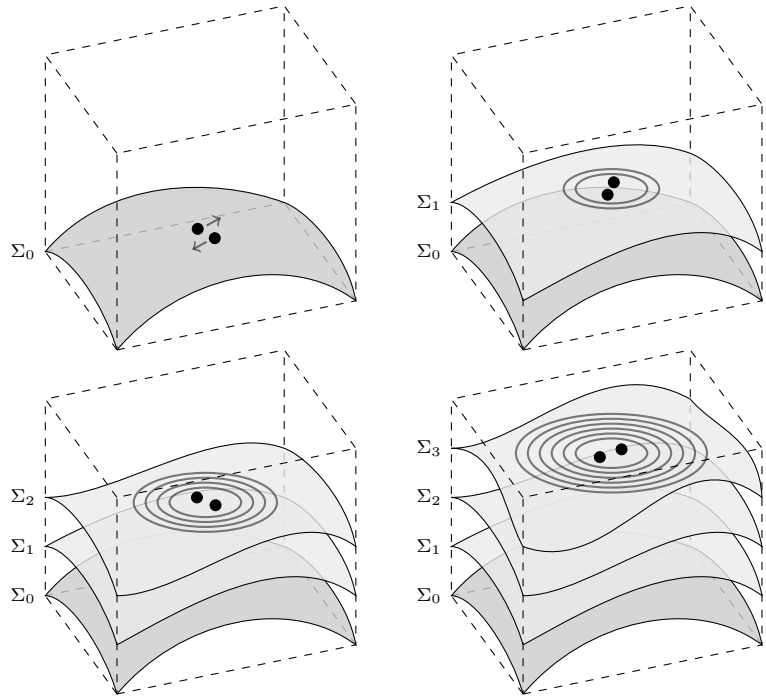

FIGURE 3. Comic impression of a binary black hole simulation in the $3+1$ formulation of general relativity.

Here ρ denotes the energy density, S_{ij} the stress tensor and S its trace, associated with the matter sources, as measured by Eulerian observers. These are observers living on world lines normal to the slices. R_{ij} denotes the spatial Riemann tensor associated with γ_{ij}. For later use we also write out the resulting evolution equation for the trace of the extrinsic curvature:

$$\partial_t K = -\gamma^{ij} D_i D_j \alpha + \alpha\big(K_{ij}K^{ij} + 4\pi(\rho + S)\big) + \beta^i D_i K. \tag{6}$$

Together (4) and (5) are called the ADM evolution equations, after Arnowitt, Deser and Misner; cf [4]. The form in which they are presented here is due to a reformulation by York though; cf [49] and the discussion in [1, p 75f]. The constraint equations on the other hand are given by

constraint equations

$$R + K - K_{ij}K^{ij} = 16\pi\rho, \tag{7}$$

$$D_j(K^{ij} - \gamma^{ij}K) = 8\pi j^i, \tag{8}$$

where R denotes the spatial Ricci scalar associated with γ_{ij} and K the trace of the extrinsic curvature on the slices. j^i denotes the momentum density as measured by Eulerian observers. (7) and (8) are called the Hamiltonian and momentum constraint respectively, and together they build the Einstein constraints.

Together (4), (5), (7) and (8) can be viewed as a $3+1$ formulation of the Einstein equation (1). Hence as intended, general relativity is thereby formulated as an initial data problem, where initial data is given by the specification of the dynamical quantities γ_{ij} and K_{ij} on a single slice in such a way that the constraints are satisfied. The evolution equations then prescribe how this data evolves with time, ie how it changes from one slice to the next. Figure 3 illustrates this with the example of a binary black hole problem.

constrained and free data

$\{\gamma_{ij}, K^{ij}\}$ has twelve independent components in total, and there are four constraint equations (7) and (8). Hence, in principle one could construct initial data

by directly prescribing eight components such that they correspond to the physical situation we are looking at, and by solving the constraints for the other four. However in general it is non-trivial to specify the free data in such a direct way. It turned out to be fruitful to formulate the constraints in terms of other, related, quantities, which allow for a clearer specification of the free data, and from which the true physical initial data can be reconstructed. There are several successful approaches. Most of them introduce a conformally related spatial metric and extrinsic curvature, and then differ in how the latter is further decomposed. In the following section we discuss the weighted transverse decomposition, which is particularly suited to construct (quasi) equilibrium initial data. After that we will discuss the conformal thin-sandwich and conformal transverse decompositions as special cases.

4. The weighted transverse decomposition

We will from now always refer to spatial quantities unless indicated otherwise.

Let A_{ij} be the traceless part of the extrinsic curvature K_{ij}, ie

$$A_{ij} = K_{ij} - \frac{K}{3}\gamma_{ij}.$$

Further we introduce a scalar function ψ, the conformal factor, and define conformally related quantities to the (spatial) metric γ_{ij} and A_{ij} by

conformal relation

$$\gamma_{ij} =: \psi^4\bar{\gamma}_{ij} \quad \text{and} \quad A_{ij} =: \psi^{-2}\bar{A}_{ij}. \tag{9}$$

The exponents of ψ are chosen for convenience; cf [1, p 93, 94; in particular eq (3.2.10)]. The respective quantities with pulled indices are defined in such a way that indices of conformally related quantities are pulled by the conformal metric; eg $\gamma^{ij} =: \psi^{-4}\bar{\gamma}^{ij}$ and $A^{ij} =: \psi^{-10}\bar{A}^{ij}$ and so forth. The weighted transverse decomposition further introduces a positive scalar weight function σ, a vector potential V^i and a symmetric trace free tensor M^{ij}; cf [35]. These have no a priori physical or geometric interpretation, however allow for a decomposition of the independent degrees of freedom into free and constraint data. The respective conformally related quantities are defined by

$$\bar{\sigma} := \psi^{-6}\sigma, \quad \bar{V}^i := V^i \quad \text{and} \quad \bar{M}^{ij} := \psi^{10}M^{ij}.$$

The conformally related traceless part of the extrinsic curvature can then be written in terms of these quantities as

$$\bar{A}^{ij} = \bar{M}^{ij} + \frac{1}{\bar{\sigma}}(\bar{L}V)^{ij}, \tag{10}$$

with the action of the longitudinal operator $\bar{L}$ given by,

$$(\bar{L}V)^{ij} := \bar{D}^iV^j + \bar{D}^jV^i - \frac{2}{3}\bar{\gamma}^{ij}\bar{D}_kV^k.$$

$\bar{D}_i$ denotes the covariant derivative with respect to the conformal metric. One can then express the constraints in terms of the new quantities as

constraints in weighted transverse decomposition

$$\bar{\gamma}^{ij}\bar{D}_i\bar{D}_j\psi - \frac{1}{8}\psi\bar{R} - \frac{1}{12}\psi^5K^2 + \frac{1}{8}\psi^{-7}\bar{A}_{ij}\bar{A}^{ij} = -2\pi\psi^5\rho, \tag{11}$$

$$(\bar{\Delta}_{\bar{L}}V)^i - (\bar{L}V)^{ij}\bar{D}_j\ln\bar{\sigma} + \bar{\sigma}\bar{D}_j\bar{M}^{ij} - \frac{2}{3}\bar{\sigma}\psi^6\bar{D}^iK = 8\pi\bar{\sigma}\psi^{10}j^i. \tag{12}$$

In the Hamiltonian constraint $\bar{A}_{ij}\bar{A}^{ij}$ is understood to be given in terms of $\bar{M}^{ij}$, $\bar{\sigma}$ and V^i by (10). In the momentum constraint we used the vector laplacian $\bar{\Delta}_{\bar{L}}$, which is given by

$$(\bar{\Delta}_{\bar{L}}V)^i := \bar{D}_j(\bar{L}V)^{ij} = \bar{D}^2V^i + \frac{1}{3}\bar{D}^i\bar{D}_jV^j + \bar{R}^i{}_jV^j.$$

Together with the matter parameters $\{\rho, j^i\}$,

$$\{\bar{\gamma}_{ij}, \bar{M}^{ij}, K, \bar{\sigma}\} \tag{13}$$

specifies the free data, and the constraints are solved for $\{\psi, V^i\}$. Note however that the constraints are coupled and in general have to be solved simultaneously. The physical data $\{\gamma_{ij}, K^{ij}\}$ can then be recovered from these quantities by

$$\gamma_{ij} = \psi^4 \bar{\psi}_{ij} \quad \text{and} \quad K^{ij} = \psi^{-10} \bar{A}^{ij} + \frac{1}{3}\gamma^{ij} K$$

together with (10).

Out of the initial data set (13), the symmetric trace-free tensor $\bar{M}^{ij}$ and the scalar weight $\bar{\sigma}$ have no a priori geometric interpretations, and neither has the vector potential V^i of the solution set. Depending on the underlying problem, it therefore can be of advantage to relate these quantities to quantities with a clear geometric interpretation, as discussed in the next section. This allows for a clearer way to choose the free data.

5. The conformal thin-sandwich decomposition

conformal thin-sandwich decomposition

The conformal thin-sandwich decomposition, cf [50], represents the special case of the weighted transverse decomposition for which

$$V^i = \beta^i, \quad \bar{\sigma} = 2\bar{\alpha}, \quad \text{and} \quad \bar{M}^{ij} = -\partial_t \bar{\gamma}^{ij}/2\bar{\alpha}. \tag{14}$$

Hence the free data set is given by

$$\{\bar{\gamma}_{ij}, \partial_t \bar{\gamma}_{ij}, K, \bar{\alpha}\},$$

together with the matter parameters, and the constraints are solved for $\{\psi, \beta^i\}$. Therefore all quantities in the initial data and constraint data sets have a clear geometric interpretation. In more detail: by associating the symmetric trace-free tensor $\bar{M}^{ij}$ with the time derivative of the conformal metric $\partial_t \bar{\gamma}_{ij}$, and the scalar weight $\bar{\sigma}$ with a lapse $\bar{\alpha}$, one ends up solving the momentum constraint for a corresponding shift β^i. The respective correspondence can be seen from the time evolution equation for the conformal metric, which we get by inserting (14) into (10):

$$\bar{A}^{ij} = \frac{1}{2\bar{\alpha}} \left((\bar{L}\beta)^{ij} - \partial_t \bar{\gamma}^{ij} \right) \quad \Leftrightarrow \quad \partial_t \bar{\gamma}^{ij} = (\bar{L}\beta)^{ij} - 2\bar{\alpha}\bar{A}^{ij}. \tag{15}$$

That means that the gauge functions $\{\bar{\alpha}, \beta^i\}$ used in the conformal thin-sandwich equations are such that they are consistent with the initial change in the conformal metric $\partial_t \bar{\gamma}_{ij}$ specified in the free data set.

Clearly the physical initial data slice constructed, ie the initial data set $\{\gamma_{ij}, K^{ij}\}$, in the end relies neither on the specific gauge, nor on the specified initial change of the conformal metric with time, used in the conformal-thin sandwich formulation. And of course one is not obliged to use this gauge in a time evolution. However, one may very well make use of this feature of the decomposition to simultaneously derive a gauge, together with the initial data, which yields a desired evolution. The obvious example for such a case is stationary or quasi-stationary initial data. That is, initial data for which $\{\partial_t \gamma_{ij} = 0, \partial_t K^{ij} = 0\}$ throughout the evolution or on the initial data slice. The gauge which yields a stationary evolution is referred to as the Killing gauge, a name derived from the notion of Killing vector fields in the treatment of symmetries in differential geometry; cf [46, section C.3]. As we will see in section 3, trumpet initial data is an example of stationary initial data, when evolved with the corresponding Killing gauge.

stationary and quasi-stationary initial data, Killing gauge

If one attempts to derive a certain gauge together with the initial data, using the conformal thin-sandwich decomposition, one might rather want to solve for the lapse instead of providing it as part of the free data set. One can do this by utilising

the time evolution equation for the trace of the extrinsic curvature (6) together with the Hamiltonian constraint (7) to derive an elliptic equation for the lapse $\bar{\alpha}$; cf [1, p 103f] or [8, p 77f]:

$$\bar{D}^2(\psi^7\bar{\alpha}) = (\psi^7\bar{\alpha})\left(\frac{7}{8}\psi^{-8}\bar{A}_{ij}\bar{A}^{ij} + \frac{5}{12}\psi^4 K^2 + \frac{\bar{R}}{8} + 2\pi\psi^4(\rho + 2S)\right) - \psi^5\partial_t K + \psi^5\beta^i\bar{D}_i K. \tag{16}$$

In other words, by exchanging $\bar{\alpha}$ for $\partial_t K$ in the free data set, and adding equation (16) to the constraints, one now has

extended conformal thin-sandwich decomposition

$$\{\bar{\gamma}_{ij}, \partial_t\bar{\gamma}_{ij}, K, \partial_t K\}$$

as the free data set, and the constraints are solved for $\{\psi, \bar{\alpha}, \beta^i\}$. This approach is called the extended conformal thin-sandwich decomposition.

We conclude this chapter by stating in summary that the weighted transverse decomposition and the original conformal thin-sandwich decomposition can be regarded as virtually identical. The only difference is that in the latter case the data $\{\bar{\sigma}, V^i, \bar{M}^{ij}\}$ is given clear geometric interpretation, ie $\{\bar{\alpha}, \beta^i, \partial_t\bar{\gamma}_{ij}\}$, which however only applies to a hypothetical time evolution of the initial data constructed with the approach, not to the physical initial data $\{\gamma_{ij}, K^{ij}\}$ itself.

CHAPTER 3

Initial data for black hole simulations

excision and moving punctures

The first stable simulations capturing the in-spiral, merger and ring-down of binary black holes in coalescence, and the gravitational waves extracted from this system, was achieved in 2005; cf [37, 17, 5]. Two approaches succeeded. One is the excision method, in which the black hole horizons are tracked throughout the evolution, and declared as the inner boundaries of the numerical grid; cf [43]. The black hole singularities are thereby artificially excised from the numerical domain. On the other hand, there is the moving puncture method in which the singularities are avoided in a more natural way by virtue of the chosen gauge and evolution equations. At the time of writing, both methods still exhibit their individual advantages and disadvantages – both on a technical level and in their applicability. We will focus exclusively on the moving puncture method here. In section 1 we show how standard black hole initial data is constructed as wormhole data in the moving puncture approach. Section 2 discusses how these slices change from wormholes to trumpets by virtue of the applied gauge conditions, and how this motivates the construction of trumpet initial data. Finally, in section 3 we summarise the current status of research on trumpet initial data. This then also marks the starting point of the new work presented in this thesis.

1. Wormhole initial data

Initial data for black hole simulations using the moving puncture approach are typically provided as a slice of wormhole geometry. We shall illustrate the defining features of such a slice with the example of Schwarzschild spacetime. In a Penrose diagram, a wormhole slice joins spatial infinity of the physical half of the Kruskal-Szekeres extension i^0_R to spatial infinity of the nonphysical half i^0_L through a throat of finite area; cf figure 4. The standard Schwarzschild wormhole foliation is given by isotropic coordinates $\{x^\mu\} = \{t, r, \theta, \phi\}$. It can be obtained from Schwarzschild coordinates $\{x^{\mu'}\} = \{t', r', \theta', \phi'\}$ by the transformation

Schwarzschild in isotropic coordinates

$$t' = t, \quad r' = \psi^2 r, \quad \theta' = \theta \quad \text{and} \quad \phi' = \phi, \quad \text{with} \quad \psi = 1 + \frac{m}{2r}. \tag{17}$$

The resulting foliation $\{\alpha, \beta^i, \gamma_{ij}\}$ is then given by

$$\alpha = \frac{1 - m/2r}{1 + m/2r}, \qquad \beta^i = 0 \qquad \text{and} \qquad \gamma_{ij} = \psi^4 \bar{\gamma}_{ij}, \tag{18}$$

with

$$[\bar{\gamma}_{ij}] = \mathrm{diag}[1, r^2, r^2 \sin(\theta)^2].$$

Let us emphasise some properties. First, from (17) we can see that r' goes to infinity as r goes to infinity or 0. The former corresponds to physical spatial infinity i^0_R while the latter corresponds to spatial infinity of the non-physical half of the spacetime i^0_L. Since the latter infinity is compactified to the point $r = 0$, it is also referred to as puncture in isotropic coordinates. The throat is located at the minimum Schzwarzschild radius $r' = 2m$ which corresponds to $r = m/2$. The fact that a wormhole slice is singularity avoiding, ie that the Schwarzschild singularity $r' = 0$

puncture

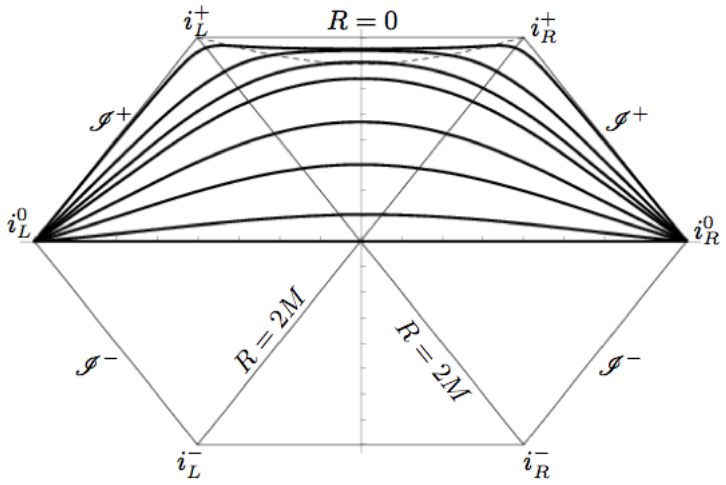

(A)

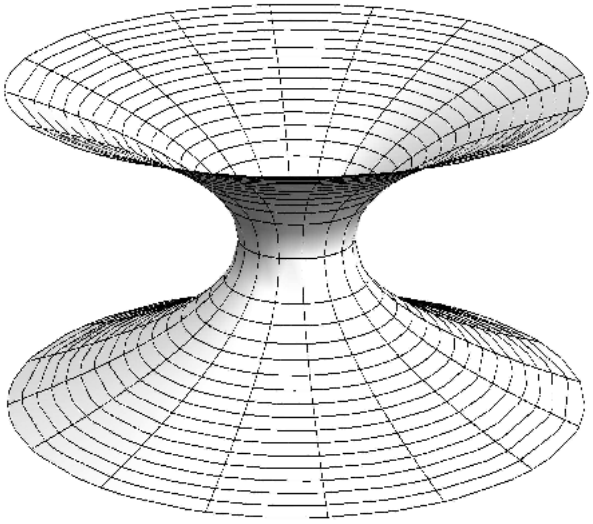

(B)

FIGURE 4. (A) shows a selection of slices of a wormhole foliation of Schwarzschild spacetime in a Penrose diagram. The embedding of a $\theta = \text{const}$ surface of one of these slices into Euclidean space is shown in (B). Both plots have been published in [24].

is not on the slice, is of primary importance to numerical simulations. Second, the slice is conformally flat since the components $\bar{\gamma}_{ij}$ are those of the flat metric in spherical coordinates. Third, from (3) we find $K_{ij} = 0$, which implies $K = 0$. It is intuitively clear that the former condition implies that the initial slice is time-symmetric, ie that it is symmetric with respect to its neighbouring slices of a time evolution. Likewise, the latter condition states that the initial slice is maximal, ie its volume element γ is extremal with respect to its neighbouring slices of a time evolution; cf [1, section 4.2.2]. To illustrate this we choose for a second an initial gauge of $\alpha = 1/2$ and $\beta^i = 0$. From the definition of the extrinsic curvature (3) we

time-symmetry and maximality

then have

$$\partial_t \gamma_{ij} = -K_{ij} \qquad \Longrightarrow \qquad \gamma^{ij}\partial_t \gamma_{ij} = -K. \tag{19}$$

Now, from Jacobi's formula for the derivative of the determinant we have

$$\partial_t \gamma = \gamma \gamma^{ij} \partial_t \gamma_{ij}.$$

Using this in (19) we find

$$-K = \partial_t \gamma / \gamma.$$

Hence, for finite γ, $K = 0$ if and only if $\partial_t \gamma = 0$, ie iff the time change of the spatial volume element is zero, which is what we wanted to show. Finally, we note that the analytical foliation $\{\alpha, \beta^i, \gamma_{ij}\}$ as given by (18) is stationary. In practice however, most numerical simulation codes cannot stably evolve a maximal wormhole initial data slice using the stationary Killing gauge $\{\alpha, \beta^i\}$ from (18). To be more precise, the codes typically have problems with a lapse that is not non-negative, which is the case here. We will elaborate on this and its practical consequences further in section 2.

multiple black hole initial data

We will focus on single black hole spacetimes in this text, but for completeness we mention that multiple black hole initial data is usually modeled as some sort of superposition of wormholes. We will not go into details here, but merely present a short summary. For more detail we refer to [1, section 3.4] and [8].

time-symmetric data – Brill-Lindquist

First, consider time-symmetric initial data, for which $K_{ij} = 0$ on the initial slice; cf [1, section 3.4.1]. For vacuum and a metric which is chosen to be conformally flat we then have a trivially satisfied momentum constraint (8) and a Hamiltonian constraint (11) given by the flat space Laplace equation

$$\bar{\gamma}^{ij}\partial_i \partial_j \psi = 0.$$

For asymptotically flat boundary conditions the following are examples of solutions:

$$\psi = 1, \qquad \psi = 1 + \frac{m}{2r}, \qquad \text{and} \qquad \psi = 1 + \sum_{\lambda=1}^{n} \frac{m_\lambda}{2|\vec{x} - \vec{x}_\lambda|}. \tag{20}$$

The first solution corresponds to a flat slice of Minkowski spacetime. The second solution corresponds to the single Schwarzschild wormhole solution of mass m with puncture at $r = 0$ as described above. Finally, the third solution corresponds to a slice with n wormhole punctures, located at the spatial coordinates x^i_λ. The bare masses m_λ differ from the ADM masses of the individual black holes for $n > 1$. The corresponding relation is given in [1, (3.4.13)]. Initial data of this type is referred to as Brill-Lindquist puncture data; cf [15]. For two black holes, these data, when evolved represents a head-on collision of two non-spinning black holes. Early simulations, using a fixed puncture approach, were already successful at evolving these data; cf [2]. Moving puncture evolutions of these data have then been performed for example in [41].

initial linear and angular momentum – Bowen-York

Of greater astrophysical relevance is initial data for multiple black holes which exhibit linear and angular momentum, in particular initial data for binary black holes in quasi-circular orbit prior to merger. In moving puncture simulation codes this is usually given as Bowen-York initial data; cf [12] as well as [1, section 3.4.2] or [8, section 12.2]. It is based on an analytical vacuum solution $V^i_{\rm BY}$ to the momentum constraint (12) for free data

$$\{\bar{\gamma}_{ij} \text{ flat}, \bar{M}^{ij} = 0, K = 0, \bar{\sigma} = 1\}, \tag{21}$$

which encodes the linear and angular momentum of a black hole at the puncture $r = 0$. The corresponding conformal extrinsic curvature $\bar{A}^{\rm BY}_{ij}$ is referred to as the Bowen-York extrinsic curvature. Since the momentum constraint is linear in this case, multiple spatially translated Bowen-York curvatures can be superposed to

represent the extrinsic curvature for multiple black holes with linear and angular momentum. Motivated by (20) the Bowen-York Hamiltonian constraint is then expected to have a solution of the form

$$\psi = 1 + \sum_{\lambda=1}^{n} \frac{m_\lambda}{2|\vec{x} - \vec{x}_\lambda|} + u, \tag{22}$$

ie of the Brill-Lindquist solution plus a deviation u; cf [13]. The individual ADM masses of the black holes are given in terms of the bare masses m_λ by [1, (3.4.32)]. In the ansatz (22), the poles of ψ at the wormhole punctures are absorbed by the analytically prescribed Brill-Lindquist part, while u is regular everywhere. The Hamiltonian constraint can then be solved for u numerically, which completes the initial data formalism.

spurious radiation

One disadvantage of Bowen-York initial data is, that it does not correspond to black holes only, but to black holes plus some spurious gravitational radiation, often referred to as junk radiation; cf for example [18]. In binary black hole simulations this junk radiation typically falls off rather quickly, and is negligible in most cases. Its contribution to the total energy and angular momentum of the spacetime however increases with the angular momenta of the black holes. This puts limits on the applicability of the moving puncture approach to high spin black hole binaries. We however point out, that it is in principle possible to produce puncture initial data that go beyond the Bowen-York solution in this regard; cf for example [28, 39, 51].

2. Trumpet initial data

In the previous section we have seen that standard moving puncture initial data models black holes as wormholes, which avoid the physical black hole singularities via their throats of finite area. When the first binary black hole moving puncture simulations succeeded in 2005, cf [17, 5], this feature of the initial data slices was well understood both numerically as well as analytically. The advances in the time evolution part of the method which lead to success were however to a greater extend guided by trial and error experimentation with different gauge conditions and evolution equations. The $1 + \log$ slicing conditions for the lapse [11] as well as a the Γ-driver shift conditions [2, 3] should be mentioned here, as well as the step to allow the conformal factor to evolve, and thereby the punctures to move across the numerical grid with the simulation [17, 5]. Hence it was less understood at the time, if and how the singularity avoidance was maintained throughout the simulation; cf for example [38].

apparent change in topology

For the case of a single Schwarzschild black hole moving puncture simulation, this question was first answered in [25]. There it was shown that the slices loose contact to the non-physical asymptotically flat end i^0_L, and asymptote to a state of stationary evolution, at which they instead terminate at a throat of finite area within the horizon, thereby still avoiding the black hole singularity; cf figure 5. In the evolution of the conformal factor ψ this transition is reflected in that its initial $\mathcal{O}(1/r)$ divergence evolves to a $\mathcal{O}(1/\sqrt{r})$ divergence. In [16] it was shown that the phenomenon is caused by a combination of the use of both, a skew grid of finite resolution, as well as of a Γ-driver shift condition, which draws the grid-points away from i^0_L and into the black hole horizon. In the limit of an infinite resolution this retraction would not occur. The numerical slices would continue to resemble a wormhole topology, however with a geometry and gauge different to that of wormholes represented by isotropic coordinates (18). Furthermore, the evolution would not be stationary.

trumpet slices

These findings suggested the construction of initial data which already exhibits the geometry to which the numerical slices would otherwise asymptote to anyway.

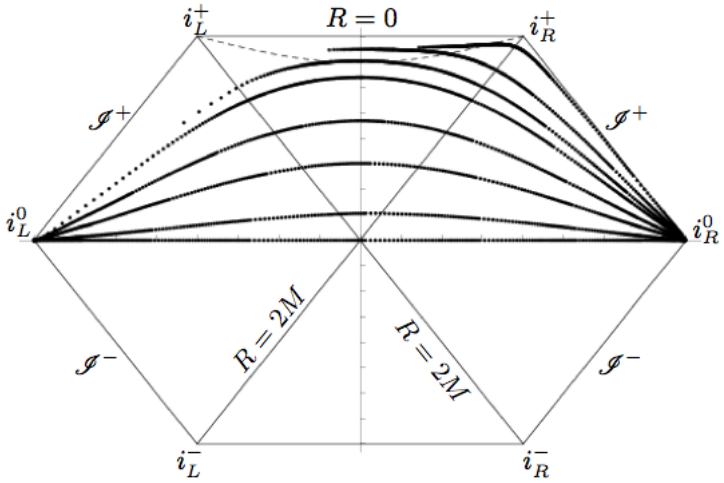

FIGURE 5. Penrose diagram showcasing the retraction of the numerical slices from i_L^0 in a moving puncture simulation of a Schwarzschild black hole. The plot shows actual simulation data and has been published in [24].

A single Schwarzschild black hole moving puncture evolution using this initial data would then be stationary right from the beginning. Because of their characteristics these proposed slices are called trumpets, or also slices with an asymptotically flat end and an asymptotically cylindrical end. The notion of trumpets extends to black hole spacetimes in general. We shall illustrate their defining features here with the example of Schwarzschild spacetime. A trumpet slice connects physical spatial infinity i_R^0 to a throat of finite area, where the slice also approaches future time-like infinity of the nonphysical half i_L^+; cf figure 6. An attempt of a more general rigorous definition can be found in [21].

maximal Schwarzschild trumpets

It turned out that a solution closely related to maximal Schwarzschild trumpets was derived and discussed in [22] by Estabrook et al in as early as 1973, both numerically and analytically, and later by alternative approaches; eg in an elegant height function approach in [9, 10] summarised in [1, section 4.3.2], or further in [33]. The potential use of these slices for numerical simulations due to their singularity avoidance via a throat has already been recognised in [22]. However, while these slices do approach i_L^+, they also still connect to i_L^0. The physical half of the Estabrook et al slices in the $t \to \infty$ limit can be regarded as representing a maximal trumpet slice though. Yet, the coordinates in which these solutions have been presented were of a form which is not suited for the moving puncture formalism of today. We quote here their stationary maximal Schwarzschild trumpet foliation $\{\alpha, \beta^i, \gamma_{ij}\}$ which is obtained as the $t \to \infty$ limit to their family of solutions. With $C = 3\sqrt{3}/4$ it is given by

$$\alpha = \sqrt{1 - \frac{2m}{r'} + \frac{C^2}{r'^4}}, \qquad \beta^{r'} = \frac{\alpha C}{r'^2} \quad \text{and} \quad \gamma_{r'r'} = \frac{1}{\alpha^2}, \tag{23}$$

and all other components are trivial, or equivalently as $\{\gamma_{ij}, K^i{}_j\}$ with

$$[K^i{}_j] = C/r'^3 \,\mathrm{diag}[2, -1, -1].$$

The lapse is zero at $r' = 3m/2$ which marks the throat, and goes to 1 at infinity, which marks the asymptotically flat end. In order to prepare this solution for the moving puncture formalism, the metric (23) has to be conformally related to the flat

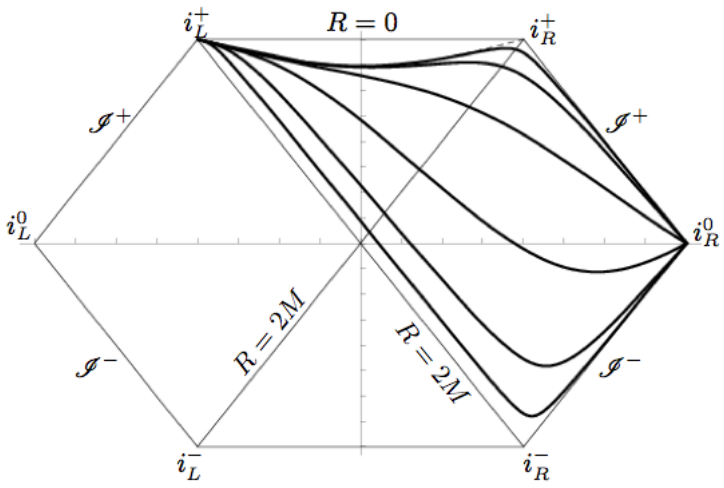

(A)

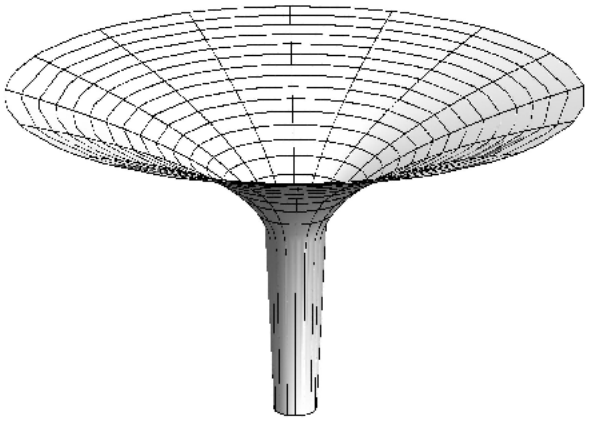

(B)

FIGURE 6. (A) shows a selection of slices of a trumpet foliation of Schwarzschild spacetime in a Penrose diagram. The embedding of a θ = const surface of one of these slices into Euclidean space is shown in (B). Both plots have been published in [24].

trumpet puncture ansatz

metric in spherical coordinates. The corresponding conformal factor has first been derived numerically in [26] by solving the Hamiltonian constraint with a trumpet puncture ansatz of the form

$$\psi = \mathcal{O}(1/\sqrt{r}) + u,$$

and where we know from (17) that the new radial coordinate r is given by

$$r' = \psi^2 r. \tag{24}$$

quasi-isotropic coordinates

Recall that a moving puncture simulation with wormhole initial data in isotropic coordinates finds the trumpet slices. Because of this relation to Schwarzschild in isotropic coordinates we call these kind of coordinates quasi-isotropic. Shortly after,

the conformal factor has been derived analytically in [7], however as function of r';

(25)
$$\psi^2 = \frac{4r'}{2r' + m + \sqrt{4r'^2 + 4mr' + 3m^2}} \left(\frac{8r' + 6m + 3\sqrt{8r'^2 + 8mr' + 6m^2}}{(4 + 3\sqrt{2})(2r' - 3m)} \right)^{1/\sqrt{2}}.$$

With (24) this also provides the transformation from the original coordinates (23) to quasi-isotropic coordinates, however only in an implicit form, since it cannot be analytically inverted to explicitly give r in terms of r'. One can then check the asymptotic behaviour

$$\lim_{r\to 0} \psi = \sqrt{\frac{3m}{2r}} \qquad \text{and} \qquad \lim_{r\to\infty} \psi = 1,$$

which, as discussed above, is characteristic to trumpets – a conformally flat end at infinity, and a throat at the trumpet puncture $r = 0$. In summary, maximal Schwarzschild trumpet moving puncture initial data is given analytically, though implicitly, by conformally relating (23) with ψ given by (25), and transforming to quasi isotropic coordinates by (24). When this data is evolved with the gauge functions (23) transformed to quasi-isotropic coordinates, the simulation is indeed stationary as also shown in [26].

$1 + \log$ Schwarzschild trumpets

These results have been expanded on in [24], where $1+\log$ Schwarzschild trumpet initial data has been derived and evolved analytically. Figure 6a is taken from there, and shows a stationary simulation of this data with $1 + \log$ and Γ-driver gauge conditions by default used in moving puncture binary black hole simulations.

3. Beyond the single Schwarzschild trumpet

The findings summarised in the previous section suggest that ideal black hole puncture initial data would be a $1 + \log$ trumpet slice of Kerr spacetime, and an according generalisation of that in the case of binary black holes. Since [24], where the essential results on single Schwarzschild trumpet puncture initial data were summarised and finalised, progress in trumpet research has been made on multiple fronts. The construction of trumpet initial data for boosted, spinning or binary black holes of Bowen-York type has been demonstrated for different cases in [27, 30, 6]. Rigorous existence and uniqueness proofs for Bowen-York trumpet solutions have been given in [19, 23, 47].

Analytical trumpet solutions for Schwarzschild black holes in [20], and for Kerr black holes in [21], have been derived recently, however in a gauge which is not suited for current numerical evolution codes – the problem to derive Kerr trumpet initial data in a suitable gauge remains open. We hope to make a significant contribution towards solving this open problem with this thesis; cf part 2.

CHAPTER 4

Numerical methods

In this chapter we outline the numerical methods which we use to solve the constraint equations in part 2. Section 1 discusses numerical grids and grid functions in one and two dimensions. We then go on to derive finite difference derivative approximations in section 2, and discuss their numerical errors. In sections 3 and 4 we show how to write partial differential equations in one and two variables in finite difference form. We also discuss how to formulate boundary conditions, and how to solve linear boundary value problems using the Thomas algorithm and successive over-relaxation. Finally, section 5 deals with linearisation and iteration to solve nonlinear boundary value problems. For further reading on numerical methods we refer to [31, 36].

Throughout this chapter, i and j denote numerical grid indices, not spatial tensor indices as in the rest of the text.

1. Finite difference grid and grid functions

Consider a function

$$h : \mathbb{R} \supset [s_{\min}, s_{\max}] \to \mathbb{R},$$
$$s \mapsto h(s).$$

For a finite difference approximation to this situation we define the discrete set of points

uniform skew grid

$$\mathbf{s} = \left\{ s \in [s_{\min}, s_{\max}] \middle| s = s_{\min} + \Delta s(i - 1/2) \; \forall i \in \{1, 2, \ldots, n\} \text{ with } 2 < n \in \mathbb{N} \right\},$$

where $\Delta s = (s_{\max} - s_{\min})/n$. We regard $\mathbf{s}$ as ordered by the index i and shall therefore also write it as a row

$$\mathbf{s} = [s_i] = [s_1, s_2, \ldots, s_n]. \tag{26}$$

$\mathbf{s}$ is called a uniform skew grid on $[s_{\min}, s_{\max}]$; uniform since its points are spaced equally with $s_{i+1} - s_i = \Delta s$ for each pair of consecutive points, and skew, or staggered, since there are no grid points on the boundaries $s_{\min}, s_{\max}$. The first and last grid points are given by $s_1 = s_{\min} + \Delta s/2$ and $s_n = s_{\max} - \Delta s/2$ respectively. We will exclusively work with uniform skew grids in part 2; uniform for simplicity, and skew to avoid divisions through zero in our numerical approximations which commonly occur on the boundaries of black hole spacetimes. In order to be able to provide boundary conditions when we solve differential equations in finite differences in part 2, we also need to define the ghost points

ghost points

$$s_0 = s_1 - \Delta s \qquad \text{and} \qquad s_{n+1} = s_n + \Delta s.$$

The grid and the ghost points are illustrated in figure 7. The finite difference approximation to h on $\mathbf{s}$ is then given by a restriction of its domain on the grid, and we will denote its values by

$$h_i = h(s_i) \quad \forall s_i \in \mathbf{s}.$$

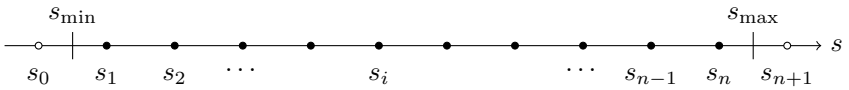

FIGURE 7. Illustration of a uniform skew grid on $[s_{\min}, s_{\max}]$ and the corresponding ghost points at the example $n = 10$.

The above definitions can be generalised to functions in two or more variables:

$$h : \mathbb{R}^2 \supset [s_{\min}, s_{\max}] \times [t_{\min}, t_{\max}] \to \mathbb{R},$$
$$(s, t) \mapsto h(s, t).$$

two dimensional grid

We then also define a grid $\mathbf{t} = [t_j] = [t_1, t_2, \ldots, t_m]$ on $[t_{\min}, t_{\max}]$ in the same way as we did for (26), and then define the grid on the whole domain as the matrix of points

$$\mathbf{S} = [(s_i, t_j)] = \begin{bmatrix} (s_1, t_1) & \cdots & (s_1, t_m) \\ \vdots & \ddots & \vdots \\ (s_n, t_1) & \cdots & (s_n, t_m) \end{bmatrix}.$$

This is illustrated in figure 8. The values of the finite difference approximation to this function are then written as

$$h_{ij} = h(s_i, t_j) \quad \forall (s_i, t_j) \in \mathbf{S}.$$

2. Finite difference derivative approximations

In order to solve differential equations in finite differences, we also need to work with finite difference approximations of derivatives. Consider the Taylor series of $h(s \pm \delta s)$ at $\delta s = 0$;

$$h(s \pm \delta s) = h(s) \pm \delta s h'(s) + \frac{\delta s^2}{2!} h''(s) \pm \frac{\delta s^3}{3!} h'''(s) + \frac{\delta s^4}{4!} h^{(4)}(s) \pm \cdots . \tag{27}$$

forward and backward derivatives

Solving for $h'(s)$ and $\delta s = \Delta s$, and evaluating at s_i yields

$$(h')_i = h'(s_i) = \frac{h(s_i + \Delta s) - h(s_i)}{\Delta s} + \mathcal{O}(\Delta s) = \frac{h_{i+1} - h_i}{\Delta s} + \mathcal{O}(\Delta s), \tag{28}$$

$$(h')_i = h'(s_i) = \frac{h(s_i) - h(s_i - \Delta s)}{\Delta s} + \mathcal{O}(\Delta s) = \frac{h_i - h_{i-1}}{\Delta s} + \mathcal{O}(\Delta s), \tag{29}$$

for the plus and minus sign respectively to lowest non-vanishing order in Δs. Dropping the higher order terms, we refer to (28) and (29) as the first forward and backward difference approximation to h' respectively; first since we truncate at lowest order, and forward or backward since we compare the value at s_i with the value at s_{i+1} or s_{i-1} respectively. The error we make due to truncation is of order Δs.

Alternatively one can use the first central approximation to h' for which the truncation error is of order Δs^2. It is obtained from (27) by forming the expression

$$h(s + \delta s) - h(s - \delta s) = 2\delta s h'(s) + \frac{\delta s^3}{3} h'''(s) + \cdots ,$$

central derivative

which can again be solved for $h'(s)$ and $\delta s = \Delta s$, and evaluated at s_i to yield

$$(h')_i = \frac{h_{i+1} - h_{i-1}}{2\Delta s} + \mathcal{O}(\Delta s^2). \tag{30}$$

Because of the higher order truncation error of the central approximation we will use it preferably to the forward and backward approximations in part 2 wherever

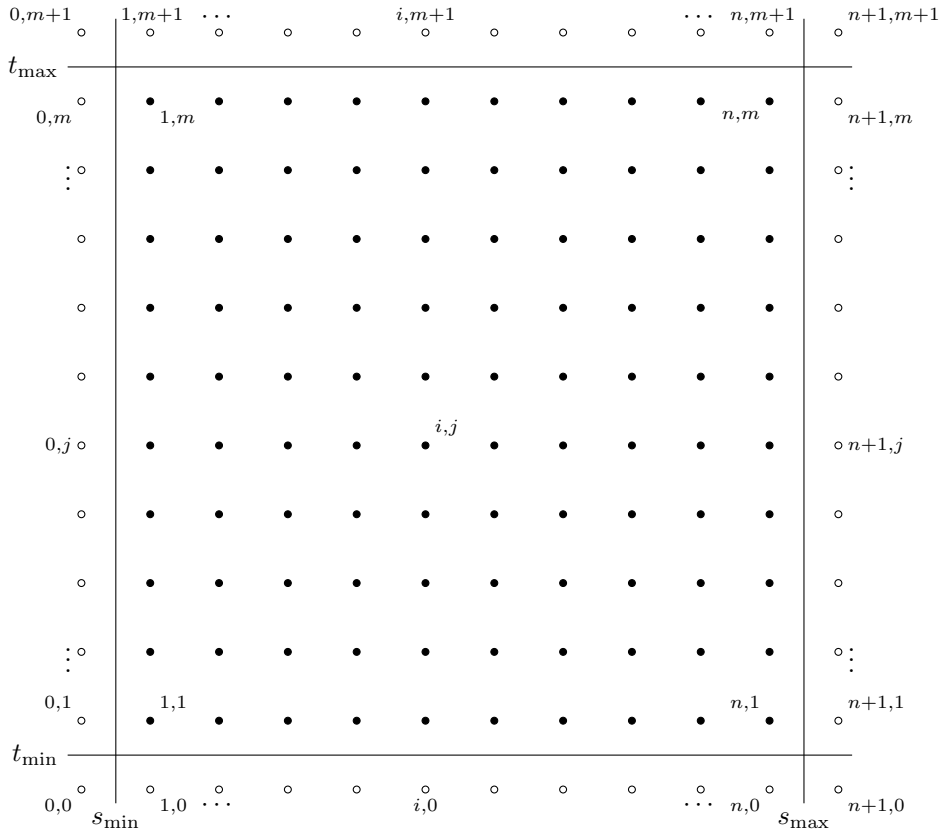

FIGURE 8. Illustration of a uniform skew grid on $[s_{\min}, s_{\max}] \times [t_{\min}, t_{\max}]$ and the corresponding ghost points. In this example $s_{\max} - s_{\min} = t_{\max} - t_{\min}$ and $n = m = 10$. Points (s_i, t_j) are labeled by their corresponding indices i, j.

possible. The approximations to higher derivatives can be obtained similarly. We quote here the result for the first central difference approximation for h'';

$$(h'')_i = \frac{h_{i+1} - 2h_i + h_{i-1}}{\Delta s^2} + \mathcal{O}(\Delta s^2). \tag{31}$$

For a derivation of this and other approximations we refer to [31, section 5.2].

optimal grid spacing

In all finite difference derivative approximations, the truncation error increases with the grid spacing Δs to some positive power. Hence, if we had infinite computing precision, then the smaller we chose Δs, the higher the accuracy of the approximation. However computing precision is finite, which introduces a roundoff error which will dominate the truncation error if Δs gets sufficiently small – for small Δs the differences in the quotients of (28), (29), (30), (31), etc, are small as well. Thus given a computing precision, then for each function and point of evaluation there is an optimal choice of Δs which yields the highest possible derivative approximation. In [31, table 5.4] this is illustrated at the example of $(\mathrm{e}^{-s})''$ evaluated at $s = 1$ using the first central approximation of the second derivative (31). For a six-digit precision the optimal approximation is achieved with $\Delta s \simeq 0.08$, while for an eight-digit precision it is achieved with $\Delta s \simeq 0.02$ in this case.

Finally, we note that the above derivative approximations can analogously be derived and applied to functions of more variables. We quote here the result for

the mixed derivative $\partial_s\partial_t$:

$$(\partial_s\partial_t h)_{ij} = \frac{h_{i+1,j+1} - h_{i+1,j-1} - h_{i-1,j+1} + h_{i-1,j-1}}{4\Delta s\Delta t} + \mathcal{O}(\Delta s^2) + \mathcal{O}(\Delta t^2).$$

3. One dimensional boundary value problems; tridiagonal matrix inversion

Consider the general, linear, second order partial differential equation (PDE) on $[s_{\min}, s_{\max}] \in \mathbb{R}$,

$$\kappa_0 + \kappa_1 h + \kappa_2 \partial_s h + \kappa_3 \partial_s^2 h = 0, \tag{32}$$

subject to some boundary conditions. Here h as well as the coefficients κ_λ are functions of s. Using the tools developed in sections 1 and 2, we can write down a finite difference approximation of this equation on a skew grid $\mathbf{s}$ of n points on the domain. Using first central approximations this yields

PDE in finite differences

$$\kappa_{0i} + \kappa_{1i} h_i + \kappa_{2i} \frac{h_{i+1} - h_{i-1}}{2\Delta s} + \kappa_{3i} \frac{h_{i+1} - 2h_i + h_{i-1}}{\Delta s^2} = 0. \tag{33}$$

The truncation error made by the approximation is of order Δs^2. This now represents a linear system of n algebraic equations. Its solution $[h_i]$ represents a finite difference approximation to the solution h of the original PDE (32). (33) can be rewritten as

$$a_i h_{i-1} + b_i h_i + c_i h_{i+1} = d_i, \tag{34}$$

with

$$a_i = \frac{\kappa_{3i}}{\Delta s^2} - \frac{\kappa_{2i}}{2\Delta s}, \qquad b_i = b_{1i} - \frac{2\kappa_{3i}}{\Delta s^2},$$
$$c_i = \frac{\kappa_{2i}}{2\Delta s} + \frac{\kappa_{3i}}{\Delta s^2}, \qquad d_i = -\kappa_{0i}.$$

boundary conditions

The equations for $i = 1$ and $i = n$ contain the values of the solution at the ghost points s_0 and s_{n+1}, ie h_0 and h_{n+1}. This is where the boundary conditions enter. Suppose we have a Dirichlet condition of value $v_{\min}$ at the lower boundary. For small grid spacing Δs this will be the average between the values of h at the first grid point and at the ghost point:

$$\frac{h_0 + h_1}{2} = v_{\min} \qquad \Longleftrightarrow \qquad h_0 = 2v_{\min} - h_1. \tag{35}$$

Entering h_0 from the latter expression into (34) for $i = 1$ we get

$$(b_1 - a_1)h_1 + c_1 h_2 = d_1 - 2v_{\min} a_1, \tag{36}$$

for the first equation. This suggests the definition of modified coefficients

$$\tilde{a}_1 = 0, \qquad \tilde{b}_1 = b_1 - a_1, \qquad \tilde{c}_1 = c_1 \quad \text{and} \quad \tilde{d}_1 = d_1 - 2v_{\min} a_1,$$

for $i = 1$, which carry the lower boundary condition. Suppose now that we have a Neumann condition of slope $w_{\max}$ at the upper boundary. Using (30) with a spacing of $\Delta s/2$ this is approximated in finite difference form by

$$\frac{h_{n+1} - h_n}{\Delta s} = w_{\max} \qquad \Longleftrightarrow \qquad h_{n+1} = \Delta s w_{\max} + h_n.$$

Entering h_{n+1} from the latter expression into (34) for $i = n$ we get

$$a_n h_{n-1} + (b_n + c_n)h_n = d_n - \Delta s w_{\max} c_n, \tag{37}$$

for the n^{th} equation. This suggests the definition of modified coefficients

$$\tilde{a}_n = a_n, \qquad \tilde{b}_n = b_n + c_n, \qquad \tilde{c}_n = 0 \quad \textit{and} \quad \tilde{d}_n = d_n - \Delta s w_{\max} c_n,$$

for $i = n$, which carry the upper boundary condition. The full system with implemented boundary conditions is now given by (36) for $i = 1$, (34) for $i = 2, 3, \dots, n-1$ and (37) for $i = n$. Together we can write this in matrix form as

tridiagonal matrix equation

$$\begin{bmatrix} \tilde{b}_1 & \tilde{c}_1 & & & 0 \\ a_2 & b_2 & c_2 & & \\ & a_3 & b_3 & \ddots & \\ & & \ddots & \ddots & c_{n-1} \\ 0 & & & \tilde{a}_n & \tilde{b}_n \end{bmatrix} \begin{bmatrix} h_1 \\ h_2 \\ \vdots \\ h_n \end{bmatrix} = \begin{bmatrix} \tilde{d}_1 \\ d_2 \\ \vdots \\ \tilde{d}_n \end{bmatrix}. \tag{38}$$

In analogy to the derivations above, a Neumann condition of slope $w_{\min}$ at the lower boundary yields the modified coefficients

$$\tilde{a}_1 = 0, \qquad \tilde{b}_1 = b_1 + a_1, \qquad \tilde{c}_1 = c_1 \quad \text{and} \quad \tilde{d}_1 = d_1 + \Delta s w_{\min} a_1,$$

while a Dirichlet condition of value $v_{\max}$ at the upper boundary yields the modified coefficients

$$\tilde{a}_n = a_n, \qquad \tilde{b}_n = b_n - c_n, \qquad \tilde{c}_n = 0 \quad \text{and} \quad \tilde{d}_n = d_n - 2v_{\max} c_n.$$

The principal form of (38) is the same in all of the discussed cases.

We now drop the tildes again, keeping in mind that the coefficients with indices 1 and n are modified. The tridiagonal form of the coefficient matrix in (38) suggests that one solves it using the Thomas algorithm; cf for example [31, section 2.4] or [36, section 2.4.1]. We shall summarise it here without derivation. First, define new coefficients consecutively as

Thomas algorithm

$$c'_i = \begin{cases} c_1/b_1 & , \quad i = 1 \\ \dfrac{c_i}{b_i - c'_{i-1} a_i} & , \quad i = 2, 3, \dots, n-1 \end{cases},$$

$$d'_i = \begin{cases} d_1/b_1 & , \quad i = 1 \\ \dfrac{d_i - d'_{i-1} a_i}{b_i - c'_{i-1} a_i} & , \quad i = 2, 3, \dots, n \end{cases}.$$

Then, obtain the solution from

$$h_i = \begin{cases} d'_n & , \quad i = n \\ d'_i - c'_i h_{i+1} & , \quad i = n-1, n-2, \dots, 1 \end{cases}.$$

4. Two dimensional boundary value problems; successive over-relaxation

Consider the general linear PDE on $[s_{\min}, s_{\max}] \times [t_{\min}, t_{\max}] \in \mathbb{R}^2$,

$$b_0 + b_1 h + b_2 \partial_s h + b_3 \partial_t h + b_4 \partial_s \partial_t h + b_5 \partial_s^2 h + b_6 \partial_t^2 h = 0, \tag{39}$$

subject to some boundary conditions. Here h as well as the coefficients b_λ are functions of s and t. Using the tools developed in sections 1 and 2, we can write down a finite difference approximation of this equation on a skew grid $\mathbf{S}$ of nm points on the domain. Using first central approximations this yields

PDE in two variables in finite differences

$$\begin{aligned} b_{0ij} + b_{1ij} h_{ij} + b_{2ij} \frac{h_{i+1,j} - h_{i-1,j}}{2\Delta s} + b_{3ij} \frac{h_{i,j+1} - h_{i,j-1}}{2\Delta t} \\ + b_{4ij} \frac{h_{i+1,j+1} - h_{i+1,j-1} - h_{i-1,j+1} + h_{i-1,j-1}}{4\Delta s \Delta t} \\ + b_{5ij} \frac{h_{i+1,j} - 2h_{ij} + h_{i-1,j}}{\Delta s^2} + b_{6ij} \frac{h_{i,j+1} - 2h_{ij} + h_{i,j-1}}{\Delta t^2} = 0. \end{aligned} \tag{40}$$

The truncation errors made by the approximation is of order Δs^2 and Δt^2. This now represents a linear system of nm algebraic equations. Its solution $[h_{ij}]$ represents a finite difference approximation to the function h of the original PDE (39).

In section 1 of chapter 7 we will use the Mathematica built in LinearSolve command using the method Banded to solve the system (40). In sections 2 and 3 of chapter 7 we will use successive over-relaxation (SOR). We shall outline this technique here. For more on the method we refer to [36, section 20.5] and [8, section 6.2.2]. The coefficient of h_{ij} in (40) is given by

successive over-relaxation

$$a_{ij} = b_{1\,ij} - \frac{2b_{5\,ij}}{\Delta s^2} - \frac{2b_{6\,ij}}{\Delta t^2}.$$

Dividing (40) by that, and bringing all terms other than h_{ij} on the right hand side yields

$$\begin{aligned} h_{ij} = \frac{-1}{a_{ij}}\Bigg(& b_{0\,ij} + b_{2\,ij}\frac{h_{i+1,j} - h_{i-1,j}}{2\Delta s} + b_{3\,ij}\frac{h_{i,j+1} - h_{i,j-1}}{2\Delta t} \\ & + b_{4\,ij}\frac{h_{i+1,j+1} - h_{i+1,j-1} - h_{i-1,j+1} + h_{i-1,j-1}}{4\Delta s\Delta t} \\ & + b_{5\,ij}\frac{h_{i+1,j} + h_{i-1,j}}{\Delta s^2} + b_{6\,ij}\frac{h_{i,j+1} + h_{i,j-1}}{\Delta t^2}\Bigg). \end{aligned} \tag{41}$$

Finally, bringing also h_{ij} on the right hand side we get

$$0 = \text{rhs}\,(41) - h_{ij}. \tag{42}$$

The right hand side of this equation expresses the difference between h_{ij} directly, and h_{ij} as calculated from the values at the neighbouring grid points; ie $h_{i\pm1,j}$, $h_{i,j\pm1}$, etc. Since (42) however merely represents an algebraic reformulation of the original PDE in finite difference approximation (40), it is clearly satisfied up to errors of order Δs^2 and Δt^2 for the values of the finite difference approximation $[h_{ij}]$ to the solution h of (39). If we however enter an approximation $[h^\nu_{ij}]$ to $[h_{ij}]$, then the difference on the right hand side of (42) yields a residual

$$res^\nu_{ij} = \text{rhs}\,(41)^\nu - h^\nu_{ij}, \tag{43}$$

which specifies how close h^ν_{ij} is to h_{ij}. The idea of SOR is then to start with an initial guess h^0_{ij} of h_{ij}, and then update it following the iterative scheme

$$h^{\nu+1}_{ij} = h^\nu_{ij} + \omega\, res^\nu_{ij}, \tag{44}$$

starting from $\nu = 0$ until a convergence criterion is met. The here introduced SOR parameter $\omega \in (0, 2)$ can be tweaked to improve the speed of convergence.

boundary conditions

The boundary conditions enter the solution scheme (44) via the residual since its expression (43) contains the values at the ghost points for $i = 1$, $i = n$, $j = 1$ or $j = m$. In analogy to what was discussed in section 3 we can eliminate these values using the finite difference approximations of the boundary conditions. We show this at the example of Dirichlet conditions. First, considering figure 8, Dirichlet conditions at $s_{\min}$, $s_{\max}$, $t_{\min}$ and $t_{\max}$ yield

$$\begin{aligned} h_{0j} + h_{1j} &= 2h(s_{\min}, t_j) \quad &\Longleftrightarrow \quad h_{0j} &= 2h(s_{\min}, t_j) - h_{1j}, \\ h_{n+1,j} + h_{nj} &= 2h(s_{\max}, t_j) \quad &\Longleftrightarrow \quad h_{n+1,j} &= 2h(s_{\max}, t_j) - h_{nj}, \\ h_{i0} + h_{i1} &= 2h(s_i, t_{\min}) \quad &\Longleftrightarrow \quad h_{i0} &= 2h(s_i, t_{\min}) - h_{i1}, \\ h_{i,m+1} + h_{im} &= 2h(s_i, t_{\max}) \quad &\Longleftrightarrow \quad h_{i,m+1} &= 2h(s_i, t_{\max}) - h_{im}, \end{aligned} \tag{45}$$

for the values at the ghost points across the edges. Yet left to specify are the values at the corner ghost points, ie h_{00}, $h_{n+1,0}$, $h_{0,m+1}$ and $h_{m+1,m+1}$. Again with the help of figure 8, for h_{00} we have

$$h_{00} + h_{01} = 2h(-\Delta s/2, t_{\min}),$$

and thus

$$\begin{aligned} h_{00} &= 2h(-\Delta s/2, t_{\min}) - h_{01} \\ &\overset{(45)}{=} 2h(-\Delta s/2, t_{\min}) - 2h(s_{\min}, t_1) + h_{11}, \end{aligned} \tag{46}$$

where in the last step we used the first equation of (45) to substitute for h_{01}. Assuming now that $h(s, t_{\min}) - h(s_{\min}, t_{\min})$ is odd we have

$$h(-\Delta s/2, t_{\min}) + h(\Delta s/2, t_{\min}) = 2h(s_{\min}, t_{\min}),$$

and thus

$$\begin{aligned} h(-\Delta s/2, t_{\min}) &= 2h(s_{\min}, t_{\min}) - h(\Delta s/2, t_{\min}) \\ &= 2h(s_{\min}, t_{\min}) - \frac{h_{11} + h_{10}}{2} \\ &\overset{(45)}{=} 2h(s_{\min}, t_{\min}) - \frac{h_{11} + 2h(s_1, t_{\min}) - h_{11}}{2} \\ &= 2h(s_{\min}, t_{\min}) - h(s_1, t_{\min}), \end{aligned} \tag{47}$$

where in the third line we used the third equation of (45) to substitute for h_{10}. Finally, using (47) in (46) we find

$$h_{00} = 4h(s_{\min}, t_{\min}) - 2h(s_1, t_{\min}) - 2h(s_{\min}, t_1) + h_{11} \tag{48}$$

for the value at the corner ghost point (s_0, t_0). In an analogous derivation we find

$$\begin{aligned} h_{0,m+1} &= 4h(s_{\min}, t_{\max}) - 2h(s_1, t_{\max}) - 2h(s_{\min}, t_m) + h_{1m}, \\ h_{n+1,0} &= 4h(s_{\max}, t_{\min}) - 2h(s_n, t_{\min}) - 2h(s_{\max}, t_1) + h_{n1}, \\ h_{n+1,m+1} &= 4h(s_{\max}, t_{\max}) - 2h(s_n, t_{\max}) - 2h(s_{\max}, t_m) + h_{mn}. \end{aligned} \tag{49}$$

for the remaining three corner ghost points at (s_0, t_{m+1}), $(s_{n+1}, 0)$ and (s_{n+1}, t_{m+1}). Defining now the modified residual $\widetilde{res}_{ij}^{\nu}$ by using the obtained relations (45), (48) and (49) to substitute for the values at the ghost points in res_{ij}^{ν}, our final solution scheme, which takes into account the boundary conditions, becomes

$$h_{ij}^{\nu+1} = h_{ij}^{\nu} + \omega\, \widetilde{res}_{ij}^{\nu}. \tag{50}$$

5. Linearisation of nonlinear equations

So far we only discussed linear PDEs. Nonlinear PDEs can often be solved by iteratively solving their linearisations. We demonstrate this at the example of the nonlinear PDE for the modified metric perturbation g, which we are going to encounter in section 1 of chapter 7;

$$d_0 + d_1 g + d_2 \partial_s g + d_3 \partial_s \partial_t g + d_4 \frac{\partial_s g \partial_t g}{1 + t(1-t)g} + d_5 \frac{g \partial_s g}{1 + t(1-t)g} = 0. \tag{51}$$

Consider the left hand side of this equation to be defined by a functional of g and its derivatives;

$$F[g, \partial_s g, \partial_t g, \partial_s \partial_t g] = \text{lhs}\,(51).$$

The linearisation of F at $(g, \partial_s g, \partial_t g, \partial_s \partial_t g)$ is then given by the first order Taylor series

$$F[g, \partial_s g, \partial_t g, \partial_s \partial_t g] + \frac{\delta F}{\delta g}\delta g + \frac{\delta F}{\delta \partial_s g}\delta \partial_s g + \frac{\delta F}{\delta \partial_t g}\delta \partial_t g + \frac{\delta F}{\delta \partial_s \partial_t g}\delta \partial_s \partial_t g.$$

Assuming that the variation commutes with the partial derivatives, ie $\delta \partial_s g = \partial_s \delta g$, etc, this yields

$$b_0 + b_1 \delta g + b_2 \partial_s \delta g + b_3 \partial_t \delta g + b_4 \partial_s \partial_t \delta g = 0, \tag{52}$$

with

$$
\begin{aligned}
b_0 &= F[g, \partial_s g, \partial_t g, \partial_s \partial_t g], \\
b_1 &= d_1 - d_5 \frac{t(1-t) g \partial_s g}{\big(1 + t(1-t)g\big)^2} - d_4 \frac{t(1-t) \partial_s g \partial_t g}{\big(1 + t(1-t)g\big)^2} + d_5 \frac{\partial_s g}{1 + t(1-t)g}, \\
b_2 &= d_2 + d_5 \frac{g}{1 + t(1-t)g} + d_4 \frac{\partial_t g}{1 + t(1-t)g}, \\
b_3 &= d_4 \frac{\partial_s g}{1 + t(1-t)g}, \\
b_4 &= d_3.
\end{aligned} \tag{53}
$$

(52) represents a linear PDE for the variation δg. Its coefficients b_λ are functionals of g and its derivatives. The original nonlinear PDE (51) can now be solved by the iterative scheme

$$g^{\iota+1} = g^\iota + \delta g^\iota,$$

starting from an initial guess g^0, and where δg^ι is obtained by solving the linear PDE (52) at each iteration step.

Part 2

Towards a numerical derivation of maximal Kerr trumpet initial data

CHAPTER 5

The approach: maximal extreme Kerr trumpets in three steps

In this chapter we outline the approach by which we work towards a numerical derivation of maximal Kerr trumpet initial data. Section 1 covers the underlying initial data system for basic choices such as vacuum, maximality and axial symmetry, and we identify the two main challenges: solving for the conformal metric, further elaborated on in section 2, and choosing appropriate boundary conditions, further discussed in section 3. Finally, we present the Kerr metric in quasi-isotropic coordinates in section 5, and point out properties which will be of use later. In particular, we will support the claim that the slices of extreme Kerr in quasi-isotropic coordinates are maximal trumpets.

1. The basic initial data system

As outlined in chapter 3, optimal black hole initial data would be a $1+\log$ trumpet slice of Kerr spacetime in quasi-isotropic coordinates. Our declared goal here is the numerical derivation of maximal Kerr trumpet initial data. As mentioned in section 1 of chapter 3, maximal means that $K = 0$. This simplifies the constraint equations significantly. At the same time, this gauge is well suited for single black hole simulations, and is closely related to the more general $1+\log$ slicing conditions which are used to evolve binary black holes; cf [11]. Since we are solving for a black-hole slice, we are in vacuum, so we have $\rho = j^i = 0$. Furthermore, as discussed in section 2 of chapter 3, single black hole trumpet data is stationary when evolved with the Killing gauge functions. As discussed in section 5 of chapter 2, this, as well as simplicity, motivates the choice $\bar{M}^{ij} = 0$. Summarising the above choices, so far we have $\{\rho = 0, j^i = 0\}$ and

impose maximality

impose vacuum

$$\{\bar{\gamma}_{ij}, \bar{M}^{ij} = 0, K = 0, \bar{\sigma}\} \tag{54}$$

for the free data set (13), and we postpone the choices for $\bar{\gamma}_{ij}$ and $\bar{\sigma}$ for now. The initial data equations in weighted transverse decomposition (11), (12) then reduce to

$$\bar{\gamma}^{ij}\bar{D}_i\bar{D}_j\psi - \frac{1}{8}\psi\bar{R} + \frac{1}{8}\psi^{-7}\bar{A}_{ij}\bar{A}^{ij} = 0, \tag{55}$$

$$(\bar{\Delta}_{\bar{L}}V)^i - (\bar{L}V)^{ij}\bar{D}_j \ln\bar{\sigma} = 0. \tag{56}$$

A further simplification to the system is made by imposing axial symmetry onto our slice, which we can, since we are solving for a slice of Kerr spacetime. Hence, all our quantities depend on two spatial coordinates only – on a radial coordinate and on a coordinate describing the polar angle.

impose axial symmetry

Our restrictions on the initial data system so far demand that we solve for an axially symmetric maximal slice of a vacuum spacetime. We yet have to make sure that it corresponds to Kerr spacetime, and that it is of trumpet geometry. To do so, on the one hand, we have to introduce mass and spin parameters m and a, and choose appropriate boundary conditions. These choices are by no means obvious. Hence, this represents the first of our main challenges. On the other hand, we

two main challenges

also have to make an appropriate choice for the conformal metric $\bar{\gamma}_{ij}$ which allows the solution to be a Kerr slice. The convenient choice of a flat conformal metric is denied since there are no conformally flat slices of Kerr spacetime; cf [44, 45]. Hence, finding a way to provide an appropriate conformal metric represents our second main challenge.

2. Solving for the conformal metric

In order to provide the conformal metric $\bar{\gamma}_{ij}$ we use an approach analogously to the one used in the extended conformal thin sandwich decomposition; cf section 5 of chapter 2. There the time evolution equation for the trace of the extrinsic curvature K is used to derive an equation which can be solved for the lapse $\bar{\alpha}$, and in the case of equilibrium or quasi-equilibrium data we could set $\partial_t K = 0$. Hence, for the price of adding a quantity $\partial_t K$ to the initial data set, and an additional equation to the constraints, one is able to solve for the lapse $\bar{\alpha}$ instead of providing it. In the following we discuss our analogous approach to solve for the conformal metric $\bar{\gamma}_{ij}$. We discuss it first in full generality, and then restrict to our case of interest.

deriving an equation for the conformal metric

We stick with the time evolution equation for the extrinsic curvature, however this time not for it's trace K, but rather for its traceless part $\bar{A}_{ij}$. We use the equation derived in [40], which is however expressed in terms of the BSSNOK conformal extrinsic curvature. We shall here denote it by a tilde. $\tilde{A}_{ij}$ has a different conformal weighting than $\bar{A}_{ij}$, cf [1, p 83, footnote 25]. The relation between the two is given by

$$\tilde{A}_{ij} = \psi^{-6}\bar{A}_{ij}.$$

Keeping this in mind we now quote [40, (2.35)]:

$$\begin{aligned}\partial_t\tilde{A}_{ij} = \psi^{-4}\Big(\alpha\Big(R_{ij} - \frac{\psi^4}{3}\bar{\gamma}_{ij}R\Big) - \Big(D_iD_j\alpha - \frac{\psi^4}{3}\bar{\gamma}_{ij}D_kD^k\alpha\Big)\Big)\\ - 2\alpha\tilde{A}_{ik}\tilde{A}_j{}^k + \bar{D}_i\beta^k\tilde{A}_{kj} + \bar{D}_j\beta^k\tilde{A}_{ki} - \frac{2}{3}\bar{D}_k\beta^k\tilde{A}_{ij} + \beta^k\bar{D}_k\tilde{A}_{ij}\\ - 8\pi\alpha\Big(\psi^{-4}S_{ij} - \frac{1}{3}\bar{\gamma}_{ij}S_k{}^k\Big).\end{aligned} \tag{57}$$

Note that here R_{ij}, R, α and D_i represent the physical quantities, not the conformally related ones. Now, instead of providing the conformal metric, we could instead choose a value for $\partial_t\tilde{A}_{ij}$ on our initial slice, and treat (57) as an additional differential equations to the constraints, which has to be solved for the conformal metric $\bar{\gamma}_{ij}$. Expressed as an extension to the weighted transverse decomposition, cf section 4 of chapter 2, the free data set is then given by

$$\{\partial_t\tilde{A}_{ij}, \bar{M}^{ij}, K, \bar{\sigma}\} \quad \text{and} \quad \{\rho, j^i, S_{ij}\}. \tag{58}$$

The set of constraints now comprises equation (57) in addition to the Hamiltonian and momentum constraints (11) and (12), and are solved for $\{\psi, V^i, \bar{\gamma}_{ij}\}$. The same extension can of course also be applied to the conformal thin sandwich, or extended conformal thin sandwich decompositions; cf section 5 of chapter 2.

Applying this now to our problem, we can dismiss the matter terms in (57) since we deal with vacuum. Further, we solve for a stationary slice, so we choose $\partial_t\tilde{A}_{ij} = 0$. Our additional equation for the conformal metric $\bar{\gamma}_{ij}$ is then given by

$$\begin{aligned}0 = \psi^{-4}\Big(\alpha\Big(R_{ij} - \frac{\psi^4}{3}\bar{\gamma}_{ij}R\Big) - \Big(D_iD_j\alpha - \frac{\psi^4}{3}\bar{\gamma}_{ij}D_kD^k\alpha\Big)\Big)\\ - 2\alpha\tilde{A}_{ik}\tilde{A}_j{}^k + \bar{D}_i\beta^k\tilde{A}_{kj} + \bar{D}_j\beta^k\tilde{A}_{ki} - \frac{2}{3}\bar{D}_k\beta^k\tilde{A}_{ij} + \beta^k\bar{D}_k\tilde{A}_{ij},\end{aligned} \tag{59}$$

which together with (55) and (56) represents our extended system of constraints. We will further break down (59) for the case of extreme Kerr in section 1 of chapter 7.

3. Finding boundary conditions

Let $r \in [0, \infty)$ be the radial coordinate and $\theta \in [0, \pi]$ be the coordinate describing the polar angle. In choosing boundary conditions for the constraint quantities ψ, V^i and $\bar{\gamma}_{ij}$, towards spatial infinity, $r \to \infty$, we are guided by asymptotic flatness. At the angular poles, $\theta = 0$ or $\theta = \pi$, we can impose symmetric boundary conditions, eg $\psi(r, -\theta) = \psi(r, \theta)$, since we have axial symmetry. The main challenge however represents the boundary at the puncture, ie at $r = 0$. This is where we have to introduce the mass and spin parameters m and a in the proper way, and impose conditions which ensure that we solve for a Kerr slice of trumpet geometry.

lower boundary condition for the Hamiltonian constraint

We start by discussing the lower boundary condition, ie $r = 0$, for the Hamiltonian constraint (55). First, we assume that for small radii r we can write the conformal factor ψ as the product of a radial dependent and an angular dependent part;

$$\psi(r, \theta) \sim \xi(r)\chi(\theta) \qquad \text{as } r \to 0. \tag{60}$$

As discussed in chapter 3 we know that for Schwarzschild and Bowen-York trumpets the conformal factor exhibits a characteristic $1/\sqrt{r}$ behaviour at the puncture, and we would assume that this also holds for Kerr. We thus set

$$\xi(r) = 1/\sqrt{r}$$

in our Ansatz (60), thereby assuming that we can pack the dependence on the black hole parameters m and a entirely into the angular dependent part χ. To deal with the angular dependence, we attempt to follow the approach taken in [27, section V]: By plugging the Ansatz (60) into the Hamiltonian constraint (55) one can derive a differential equation for χ on the interval $[0, \pi]$, for which symmetric boundary conditions can be chosen.

lower boundary condition for the momentum constraint

In order to find a lower boundary condition for the momentum constraint, we will impose that for small radii r, the quantity $\bar{A}_{ij}\bar{A}^{ij}$ for a Kerr trumpet exhibits the same behaviour as for a Bowen-York trumpet. That is

$$\bar{A}_{ij}\bar{A}^{ij} \sim \bar{A}^{\mathrm{BY}}_{ij}\bar{A}^{ij}_{\mathrm{BY}} = \frac{18M^2a^2}{r^6}\sin(\theta)^2 \qquad \text{for small } r, \tag{61}$$

where we took the expression for Bowen-York on the right hand side from [32, (4.19)]. On the other hand, with our choice of $\bar{M}^{ij} = 0$, we see from (10) that

$$\bar{A}_{ij}\bar{A}^{ij} = \frac{1}{\bar{\sigma}^2}(\bar{L}V)_{ij}(\bar{L}V)^{ij}. \tag{62}$$

The idea is then to look at this expression for small radii r and to use it together with imposition (61) in order to derive a lower boundary condition for the vector potential V^i. Note that the weight function $\bar{\sigma}$ will enter this relation – the only quantity out of the free data set (58) which has not yet been specified. We can thus attempt to choose $\bar{\sigma}$ in such a way that the above relation yields a desirable lower boundary condition for the momentum constraint (56) – a Dirichlet or Neumann condition for instance; cf section 2 of chapter 6 and section 3 of chapter 7. Before we move on there is an important point to make. The imposition (61) is motivated by the observation that slices of Kerr spacetime in quasi-isotropic coordinates satisfy this condition, which we will show in section 5; cf equation (72). It is important to note however, that while quasi-isotropic coordinates represent a trumpet foliation for extreme Kerr, they do represent a wormhole foliation for slow Kerr. We will elaborate on this at the end of section 5. The use of (61) as imposition in the

attempt to derive a slow Kerr trumpet is thus not guaranteed to yield success. However, as we pointed out in section 3 of chapter 3, Bowen-York trumpets have been rigorously proven to exist and be unique [19, 23, 47] and could be constructed numerically [27, 30, 6].

We postpone for now a discussion of how to find a lower boundary condition for the conformal metric $\bar{\gamma}_{ij}$ until section 1 of chapter 7.

4. Proceeding in three steps

In the previous sections of this chapter we outlined our approach to solve for maximal Kerr trumpet initial data and highlighted the challenges we are facing in doing it. Since in tackling these challenges we rely in part on educated guesses and approaches which are not guaranteed to yield success from several sides, we will apply our approach in three consecutive steps: first to the special case of Schwarzschild spacetime, then to the special case of extreme Kerr spacetime and finally to the case of Kerr spacetime in full generality. These special cases are on the one hand simpler than the full problem, and on the other hand also provide us with the convenience that we can compare to the analytically known data. The maximal Schwarzschild trumpet solution has been discussed in section 2 of chapter 3, and we will see that the maximal extreme Kerr trumpet is provided by Kerr in quasi-isotropic coordinates in section 5. For the Schwarzschild case we do not need to worry about a spin parameter and an angular dependence, and can also choose the conformal metric to be flat. Likewise, for extreme Kerr we have $a = m$ and thus again a one-parameter family of solutions, such as for Schwarzschild. For the extreme Kerr case we can test our approaches to solve for the conformal metric and find the angular dependence of the lower boundary conditions. But we do not have to implement all these things at once, since we can still use the analytically known solution. Hence we can first solve the system prescribing the conformal metric and all the boundary conditions, and later tackle these challenges one after the other. Finally, for the general Kerr case, we will have to introduce a spin parameter, and apply the approach to this case, where we will however not be guided by an analytic solution any longer.

5. Kerr in quasi-isotropic coordinates

In the following chapters we will work in quasi-isotropic coordinates, or a compactified version thereof. The standard coordinates in which the Kerr spacetime metric is usually introduced are the Boyer-Lindquist coordinates, which we shall denote by $\{x^{\mu'}\} = \{t', r', \theta', \phi'\}$, and the components of the metric are usually expressed in terms of auxiliary functions such as

$$\begin{aligned}\rho^2 &= r'^2 + a^2\cos(\theta')^2,\\ \Delta &= r'^2 - 2mr' + a^2,\\ \Sigma &= (r'^2 + a^2)^2 - \Delta a^2 \sin(\theta')^2.\end{aligned}$$

Kerr in Boyer-Lindquist coordinates

The component matrix of the Kerr metric in Boyer-Lindquist coordinates $[g_{\mu'\nu'}]$ is then given by

$$[g_{\mu'\nu'}] = \begin{bmatrix} g_{t't'} & 0 & 0 & g_{t'\phi'} \\ 0 & g_{r'r'} & 0 & 0 \\ 0 & 0 & g_{\theta'\theta'} & 0 \\ g_{t'\phi'} & 0 & 0 & g_{\phi'\phi'} \end{bmatrix},$$

with

$$
\begin{aligned}
g_{r'r'} &= \rho^2/\Delta, & g_{t't'} &= -(1-2mr'/\rho^2),\\
g_{\theta'\theta'} &= \rho^2, & g_{t'\phi'} &= -2mar'\sin(\theta')^2/\rho^2,\\
g_{\phi'\phi'} &= \Sigma\sin(\theta')^2/\rho^2.
\end{aligned}
\tag{63}
$$

Kerr in quasi-isotropic coordinates

The transformation to quasi-isotropic coordinates $\{x^\mu\} = \{t, r, \theta, \phi\}$ is performed by,

$$g_{\mu\nu} = \frac{\partial x^{\mu'}}{\partial x^\mu}\frac{\partial x^{\nu'}}{\partial x^\nu} g_{\mu'\nu'},$$

with

$$t' = t, \qquad r' = \Big(1+\frac{M+a}{2r}\Big)\Big(1+\frac{M-a}{2r}\Big)r, \qquad \theta' = \theta \qquad \text{and} \qquad \phi' = \phi;$$

cf [14, section II]. We pause here for a second to note, that in the special case of zero spin, ie $a = 0$, this transformation reduces to (17), ie the coordinates would then describe Schwarzschild in isotropic coordinates. Moving on, for the spacetime metric components in quasi-isotropic coordinates $[g_{\mu\nu}]$ we then have

$$
[g_{\mu\nu}] = \begin{bmatrix} g_{tt} & 0 & 0 & g_{t\phi} \\ 0 & g_{rr} & 0 & 0 \\ 0 & 0 & g_{\theta\theta} & 0 \\ g_{t\phi} & 0 & 0 & g_{\phi\phi} \end{bmatrix} = \begin{bmatrix} g_{t't'} & 0 & 0 & g_{t'\phi'} \\ 0 & (\frac{\partial r'}{\partial r})^2 g_{r'r'} & 0 & 0 \\ 0 & 0 & g_{\theta'\theta'} & 0 \\ g_{t'\phi'} & 0 & 0 & g_{\phi'\phi'} \end{bmatrix},
\tag{64}
$$

where we now view all quantities as functions of the new coordinates $\{x^\mu\}$.

α, β^i and γ_{ij} of Kerr in quasi-isotropic coordinates

From (2) we can now read off the $3+1$ foliation form $\{\alpha, \beta^i, \gamma_{ij}\}$ of the Kerr metric in quasi-isotropic coordinates; cf sections 2 and 3 of chapter 2. Calculating the inverse of (64) we find

$$g^{tt} = -\frac{g_{\phi\phi}}{g_{t\phi}^2 - g_{tt}g_{\phi\phi}} \overset{(2)}{=} -\frac{1}{\alpha^2} \quad \Rightarrow \quad \alpha = \sqrt{\frac{g_{t\phi}^2 - g_{tt}g_{\phi\phi}}{g_{\phi\phi}}}
\tag{65}$$

for the lapse, and similarly we find for the only non-vanishing component of the shift

$$g^{\phi\phi} = \frac{g_{t\phi}}{g_{t\phi}^2 - g_{tt}g_{\phi\phi}} \quad \Rightarrow \quad \beta^\phi = g^{\phi\phi}\beta_\phi \overset{(2)}{=} \frac{g_{t\phi}^2}{g_{t\phi}^2 - g_{tt}g_{\phi\phi}}.
\tag{66}$$

Finally, for the spatial metric component matrix we find

$$[\gamma_{ij}] \overset{(2)}{=} \mathrm{diag}[g_{rr}, g_{\theta\theta}, g_{\phi\phi}] \underset{(63)}{\overset{(64)}{=}} \mathrm{diag}\left[\frac{\rho^2}{r^2}, \rho^2, \frac{\Sigma}{\rho^2}\sin(\theta)^2\right].
\tag{67}$$

ψ and $\bar{\gamma}_{ij}$ of Kerr in quasi-isotropic coordinates

Defining the conformal factor as

$$\psi = \sqrt{\rho/r},
\tag{68}$$

from (9) we then have

$$[\bar{\gamma}_{ij}] = \mathrm{diag}\left[1, r^2, \frac{\Sigma}{\rho^4}r^2\sin(\theta)^2\right] = \mathrm{diag}[1, r^2, r^2\sin(\theta)^2(1+h)],
\tag{69}$$

where in the last step we defined the auxiliary function $h(r, \theta)$ as

$$h = \Sigma/\rho^4 - 1.
\tag{70}$$

h as perturbation from conformal flatness

Note that h represents the deviation from conformal flatness, since if it was zero, then $\bar{\gamma}_{ij}$ would reduce to the flat metric in spherical coordinates. We will capitalise on that in section 1 of chapter 7, when we solve for the conformal metric in the extreme Kerr trumpet case, and reduce the differential equation for the metric (59) to a single equation for h. We plan to do the same, and also impose a conformal metric of the form (69) in the attempt to solve for the slow Kerr trumpet. While we

can see from (69) that this indeed does hold for Kerr in quasi-isotropic coordinates in general, we again have to keep in mind that these coordinates represent a wormhole foliation for slow Kerr, not a trumpet foliation, as we will discuss at the end of this section.

$\bar{A}_{ij}$ for Kerr in quasi-isotropic coordinates

We turn our attention now to the conformally related extrinsic curvature $\bar{A}_{ij}$. Using what we have established so far in this section, it can readily be derived by (10). We quote here the result from [26, section 5]. Note however that there is a factor 2 missing on the right hand side of [26, (28)]. The non-vanishing components are given by

$$\bar{A}_{r\phi} = \frac{H_E}{r^2}\sin(\theta)^2 \qquad \text{and} \qquad \bar{A}_{\theta\phi} = \frac{H_F}{r}\sin(\theta), \tag{71}$$

with

$$H_E = \frac{1}{\sqrt{\Sigma}}\frac{ma}{\rho^2}\left((r'^2 - a^2)\rho^2 + 2r'^2(r'^2 + a^2)\right),$$
$$H_F = -\sqrt{\frac{\Delta}{\Sigma}}\frac{2ma^3 r'}{\rho^2}\sin(\theta)^2\cos(\theta).$$

From this we can then calculate the quantity $\bar{A}_{ij}\bar{A}^{ij} = \bar{A}_{ij}\bar{A}_{kl}\bar{\gamma}^{ki}\bar{\gamma}^{lj}$. We can now justify relation (61) by performing an expansion of $\bar{A}_{ij}\bar{A}^{ij}$ at $r = 0$. Using (71) this yields

$$\bar{A}_{ij}\bar{A}^{ij} \simeq \begin{cases} \dfrac{2m^4}{r^6}\sin(\theta)^2 & , \quad \text{extreme Kerr} \\ \dfrac{8m^2a^2}{r^6}\sin(\theta)^2 & , \quad \text{slow Kerr} \end{cases}, \tag{72}$$

which shows that (61) is a valid proposition for Kerr in quasi-isotropic coordinates. We note the different factors for the two cases in (72).

extreme Kerr trumpet versus slow Kerr wormhole

Let us conclude by elaborating on the claim that quasi-isotropic coordinates represent a wormhole foliation for slow Kerr, ie $a \in (0, m)$, but a trumpet foliation for extreme Kerr, ie $a = m$. We support this claim by two observations. First, consider a quasi-isotropic sphere of radius r. The metric induced by (67) onto such a sphere is given by

$$[\varphi_{ij}] = \mathrm{diag}\left[\rho^2, \frac{\Sigma}{\rho^2}\sin(\theta)^2\right],$$

and hence the area of the sphere by

$$A(r) = \int_0^{2\pi}\int_0^{\pi}\sqrt{\varphi}\,\mathrm{d}\theta\mathrm{d}\phi = 2\pi\int_0^{\pi}\sqrt{\Sigma}\sin(\theta)\,\mathrm{d}\theta. \tag{73}$$

Expanding $\sqrt{\Sigma}$ in a Taylor series at $r = 0$ yields

$$\sqrt{\Sigma} \simeq \begin{cases} 2m^2 & , \quad \text{extreme Kerr} \\ \dfrac{(m^2 - a^2)^2}{16r^2} & , \quad \text{slow Kerr} \end{cases},$$

to lowest order. From (73) we thus have

$$A(0) \begin{cases} = 8\pi m^2 & , \quad \text{extreme Kerr} \\ \to \infty & , \quad \text{slow Kerr} \end{cases}.$$

This is consistent with the claim. While $r = 0$ represents spatial infinity at the other end of the wormhole for slow Kerr, it represents a throat of finite area $8\pi m^2$

for extreme Kerr. Second, consider the behaviour of the conformal factor for small radii r. An expansion of (68) at $r = 0$ yields

$$\psi \simeq \begin{cases} \dfrac{\left(m^2(1+\cos(\theta)^2)\right)^{1/4}}{\sqrt{r}} & , \quad \text{extreme Kerr} \\ \dfrac{\left((m^2-a^2)^2\right)^{1/4}}{2r} & , \quad \text{slow Kerr} \end{cases} . \tag{74}$$

So for small r we see that for extreme Kerr ψ is of order $1/\sqrt{r}$, which is characteristic to a trumpet, while for slow Kerr ψ is of order $1/r$, which is characteristic to a wormhole; cf section 2 of chapter 3.

CHAPTER 6

A numerical derivation of maximal Schwarzschild trumpet initial data

I this chapter we present the first of our main results of this thesis: a numerical derivation of maximal Schwarzschild trumpet initial data in the weighted transverse decomposition. The analytical maximal trumpet solution is available in this case, and we discussed it in section 2 of chapter 3; cf (23). The goal of this chapter, is however not the mere reproduction of this result, but rather to do it in an approach that can be generalised for the cases of maximal extreme Kerr and Kerr trumpets. We will thus only make nontrivial use of the analytic solution in two cases, and otherwise act as if we would not have an analytical solution available. Those cases are the imposition of the following asymptotic behaviours,

$$\bar{A}_{ij}\bar{A}^{ij} \sim \frac{81}{8}\frac{m^4}{r^6} \quad \text{as} \quad r \to 0, \tag{75}$$

$$\psi \sim \sqrt{\frac{3m}{2r}} \quad \text{as} \quad r \to 0. \tag{76}$$

These will serve to choose proper physical boundary conditions that ensure that we solve for a trumpet slice of a Schwarzschild black hole of mass m. We have seen in section 5 of chapter 5, that both of these relations have a generalisation in extreme Kerr; cf (61) and (74). We have also discussed there, that extreme Kerr in quasi isotropic coordinates represents a maximal trumpet foliation. We thus build our approach on the assumption that these relations have generalisations in the maximal slow Kerr trumpet case as well, and that we can find them.

In section 1 we lay out the initial data system for maximal Schwarzschild trumpets in the weighted transverse decomposition. We also discuss how to solve for the Killing gauge functions which yield a stationary evolution, and discuss the solution process. In the following sections we then solve each of these equations consecutively.

1. The maximal Schwarzschild trumpet initial data system

The basic initial data system laid out in section 1 of chapter 5 further simplifies for Schwarzschild. First, we can choose the metric to be conformally flat for convenience. Second, we have no angular momentum, ie $a = 0$. Hence the mass m is the only parameter characterising the family of solutions. We can also choose spherical coordinates $\{r, \theta, \phi\}$ to adapt to the spatial symmetry, and we can expect all quantities to depend on r only. Finally, we make our choice of the weight function $\bar{\sigma}$, with which our free data set (54) becomes

$$\left\{ [\bar{\gamma}_{ij}] = \mathrm{diag}[1, r^2, r^2 \sin(\theta)^2], \bar{M}^{ij} = 0, K = 0, \bar{\sigma} = \frac{r^2}{1+r^2} \right\}, \tag{77}$$

together with vanishing matter parameters $\{\rho = 0, j^i = 0\}$. We will elaborate on the choice of $\bar{\sigma}$ in section 2 when we point out its connection to the lower boundary condition for the momentum constraint – recall the discussion in section 3 of chapter 5 surrounding imposition (61).

Schwarzschild trumpet initial data system

With (77), the basic initial data system {(55), (56)} then reduces to

$$\Delta_r \psi + \frac{1}{8}\psi^{-7}\bar{A}_{ij}\bar{A}^{ij} = 0, \tag{78}$$

$$\Delta_r V^r - \frac{2}{r^2}V^r - \frac{3}{4}\bar{A}^{rr}\partial_r\bar{\sigma} = 0, \tag{79}$$

with

$$\bar{A}^{rr} = \frac{4}{3\bar{\sigma}}\left(\partial_r V^r - \frac{1}{r}V^r\right) \quad \text{and} \quad \bar{A}_{ij}\bar{A}^{ij} = \frac{8}{3\bar{\sigma}^2}\left(\partial_r V^r - \frac{1}{r}V^r\right)^2. \tag{80}$$

$\Delta_r\,.\equiv \frac{1}{r^2}\partial_r(r^2\partial_r\,.\,)$ denotes the radial part of the flat space Laplace operator, and (80) follows directly from (10) with $\bar{M}^{ij} = 0$. All coordinate functions depend on r only, and the vector potential V^i has a non-trivial radial component only, due to spherical symmetry.

Equations (78) and (79) together represent a system of two coupled one-dimensional ordinary elliptic differential equations for the constrained data $\{\psi, V^r\}$. The physical initial data $\{\gamma_{ij}, K^{ij}\}$ can then be reconstructed by,

$$\gamma_{ij} = \psi^4\bar{\psi}_{ij} \quad \text{and} \quad K^{ij} = \psi^{-10}\bar{A}^{ij} \quad \text{with} \quad \bar{A}^{ij} = \frac{1}{\bar{\sigma}}(\bar{L}V)^{ij}. \tag{81}$$

In addition to the constrained data $\{\psi, V^i\}$, which specifies the initial data slice, we would also like to find the Killing gauge functions $\{\alpha, \beta^i\}$ by virtue of which this data is evolved stationary. We can find the Killing lapse α by using (16), which has been derived from (6). In the present case this reduces to

$K =$ const equation

$$\Delta_r(\psi\alpha) - \frac{7}{8}\psi^{-8}\bar{A}_{ij}\bar{A}^{ij}(\psi\alpha) = 0. \tag{82}$$

equation for β^r

We call it here the $K =$ const equation. Finally, we can find the Killing shift β^r by using the first equation of (80) in the conformal thin-sandwich case (14);

$$\partial_r\beta^r - \frac{1}{r}\beta^r = \frac{3}{2}(\psi^{-6}\alpha)\bar{A}^{rr}. \tag{83}$$

Alternatively we could get β^r by solving the momentum constraint in the conformal thin sandwich case.

The solution process is sketched in figure 9, where the equations are solved clockwise, starting from the momentum constraint. The momentum constraint is solved for the vector potential V^r, from which we can calculate $\bar{A}^{rr}$ and $\bar{A}_{ij}\bar{A}^{ij}$; cf (80). With the latter we can then solve the Hamiltonian constraint for the conformal factor ψ. ψ together with $\bar{A}_{ij}\bar{A}^{ij}$ is then fed to the $K =$ const equation in order to obtain the Killing lapse α. Finally, we use α together with $\bar{A}^{rr}$ to solve equation (83) for the Killing shift β^r.

The free data (77) only specifies that we attempt to solve for a maximal Schwarzschild initial data slice. To further ensure that we solve for a slice of trumpet geometry, we have to choose appropriate boundary conditions. We will discuss these for each equation in the respective section.

2. The momentum constraint

Following figure 9 we start with the momentum constraint (79). To begin our discussion of the boundary conditions we note that the vector potential V^r together with our chosen weight function $\bar{\sigma}$ determine the value of the extrinsic curvature, and especially of $\bar{A}_{ij}\bar{A}^{ij}$ through the second equation of (80). Therefore, our choice of boundary condition for V^r has to be consistent with the asymptotic behaviour of our choice of $\bar{\sigma}$ via this relation. As outlined in section 3 of chapter 5, we will impose the $r \to 0$ behaviour of $\bar{A}_{ij}\bar{A}^{ij}$ as (61) when we solve for the Kerr trumpet. We can thus also use the correct behaviour for Schwarzschild, without harming the

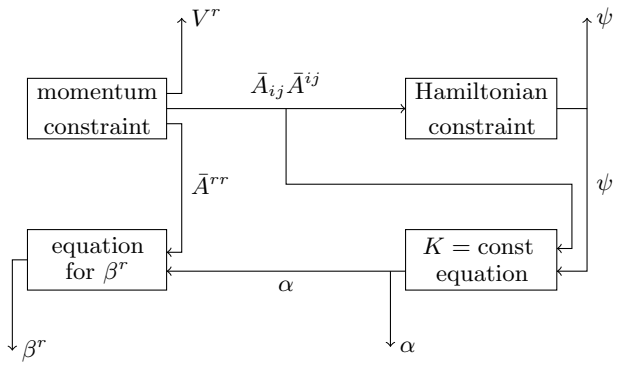

FIGURE 9. The solution process.

generalisability of the approach. From the analytic solution presented in section 2 of chapter 3, we have

impose behaviour of $\bar{A}_{ij}\bar{A}^{ij}$ for small r

$$\bar{A}_{ij}\bar{A}^{ij} \sim \frac{81}{8}\frac{m^4}{r^6} \quad \text{as} \quad r \to 0. \tag{75}$$

If we now choose

$$\bar{\sigma} \sim r^2 \quad \text{as} \quad r \to 0, \tag{84}$$

and a Taylor series Ansatz for V^r, then we find from (80) and (75) that

$$\lim_{r\to 0} V^r(r) = \frac{9\sqrt{3}}{8}m^2. \tag{85}$$

That means that a $\bar{\sigma}$ with the asymptotic behaviour (84) is consistent with the mass determined Dirichlet condition (85) for V^r at the lower boundary. For the upper boundary condition, considering asymptotic flatness, we set

$$\lim_{r\to\infty} V^r(r) = 0,$$

and we choose that

$$\bar{\sigma} \to 1 \quad \text{as} \quad r \to \infty. \tag{86}$$

While other choices may be legitimate, it is the natural choice to let the vector potential go to zero and the weight function to a constant as the slice becomes flat. Many choices may be made for $\bar{\sigma}$, which satisfy the asymptotic behaviour (84) and (86). As already anticipated in (77) we choose

$$\bar{\sigma} = \frac{r^2}{1+r^2}.$$

We note that the momentum constraint (79) is solved analytically by

results

$$V^r = \frac{9\sqrt{3}}{8}m^2\left(1 + r\left(\arctan r - \frac{\pi}{2}\right)\right). \tag{87}$$

for our choices of $\bar{\sigma}$ and boundary conditions. However, as stated in the introduction to this chapter, we attempt to develop a numerical approach which can be generalised to extreme Kerr and slow Kerr spacetime, for which an analytic solution to the momentum constraint would be difficult to derive. We thus solve the constraint numerically, using our own elliptic solver, based on tridiagonal matrix inversion using the Thomas algorithm; cf 3 of chapter 4. For this, we compactify the original domain $r \in [0, \infty)$ to $s \in [0, 1]$ by

$$r = \frac{s}{1-s}.$$

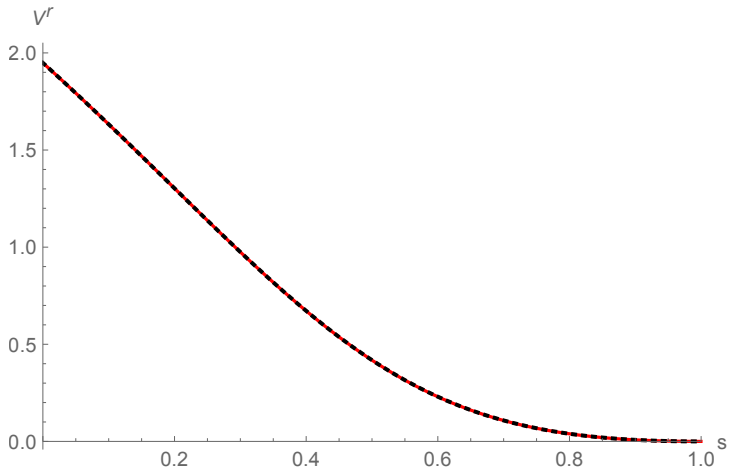

(A)

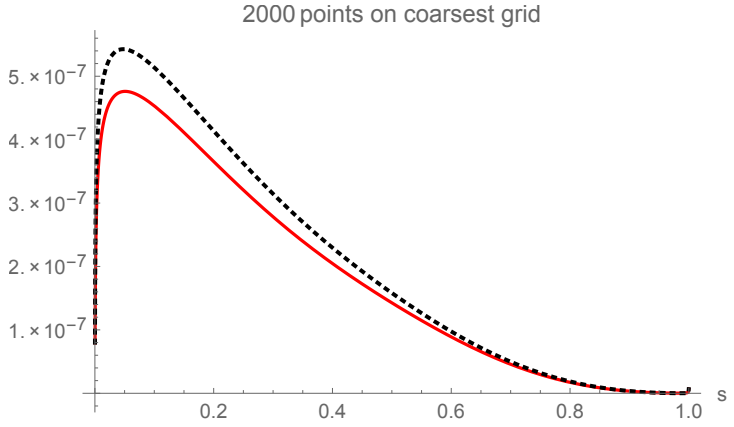

(B)

FIGURE 10. (A) shows a plot of the numerical solution $[V^r]$ produced by our solver (black, dashed) together with the analytical solution (red, line). The number of grid points is $n = 2\,000$. A second order self-convergence test is shown in (B). Denoting the interpolations of the solutions with n, $2n$ and $4n$ grid points by V^r_n, V^r_{2n} and V^r_{4n}, we have $V^r_{2n} - V^r_n$ in (red, lined) and $4(V^r_{4n} - V^r_{2n})$ in (black, dashed).

Figure 10 shows the solution produced by our solver on a uniform skew grid of 2 000 points together with the analytical solution (87), as well as a second order self-convergence test.

3. The Hamiltonian constraint

trumpet puncture ansatz

With V^r obtained from the momentum constraint, we can now calculate $\bar{A}_{ij}\bar{A}^{ij}$ from (80), and use this in the Hamiltonian constraint (78). We start by imposing the trumpet puncture ansatz

$$\psi \sim \sqrt{\frac{3m}{2r}} \quad \text{as} \quad r \to 0. \tag{76}$$

As shown in section 2 of chapter 3 for Schwarzschild, and in section 5 of chapter 5 for extreme Kerr, this $1/\sqrt{r}$ behaviour is a well established characteristics of trumpet slices, and we plan to later generalise this ansatz for Kerr.

Moving on to the boundary conditions, for the upper boundary we can clearly choose

$$\lim_{r\to\infty} \psi = 1,$$

since we solve for an asymptotically flat slice. To deal with the $\sqrt{3m/2r}$ divergence (76) at the lower boundary, we follow the approach taken in [26] and [27], and make an ansatz $\psi_0 + u$ ansatz

$$\psi = \psi_0 + u \quad \text{with} \quad \psi_0 = \frac{1}{1+r^4}\sqrt{\frac{3m}{2r}} + \frac{r^4}{1+r^4},$$

which meets the boundary conditions for ψ on both ends. The correct asymptotic behaviour is now absorbed in the analytically prescribed function ψ_0, and the Hamiltonian constrained is solved for the regular deviation u. For the latter we have the boundary conditions

$$u(0) = 0 \quad \text{and} \quad \lim_{r\to\infty} u(r) = 0.$$

We can now solve the Hamiltonian constraint with our solver using the Thomas algorithm. Note however that the constraint is nonlinear, so we have to linearise and iterate following the scheme resuts

$$u^{\iota+1} = u^{\iota} + \delta u^{\iota},$$

as discussed in section 5 of chapter 4. We start from the initial guess $u^0 = 0$. Figure 11 shows the deviation $[u]$ and the resulting solution $[\psi]$ produced by our solver on a uniform skew grid of 2 000 points, as well as a self-convergence test for second order convergence. We note that we provide $\bar{A}_{ij}\bar{A}^{ij}$ to our solver analytically for the self-convergence test to ensure that we test in isolation from errors stemming from the momentum constraint solver.

4. The Killing gauge functions

In the preceding two sections we constructed maximal Kerr trumpet initial data $\{\psi, V^r\}$ numerically in the weighted transverse decomposition. We however also want to find the Killing gauge functions $\{\alpha, \beta^r\}$ that yield a stationary evolution of this data, ie we need to solve (82) and (83). Note that all of the required functions for these equations are now provided by the solutions of the Hamiltonian and momentum constraints; cf figere 9.

We know from (23) that the lapse has to freeze, ie go to zero at the puncture $r = 0$. For the upper boundary condition we again consider asymptotic flatness. Hence we have

$$\alpha(0) = 0 \quad \text{and} \quad \lim_{r\to\infty} \alpha(r) = 1$$

as boundary conditions for (82). Likewise, for the Killing shift β^r we choose

$$\beta^r(0) = 0 \quad \text{and} \quad \lim_{r\to\infty} \beta^r(r) = 0.$$

Figure 12 shows the solutions obtained from our solvers with a grid on 2 000 points. Self-convergence tests show again clear second order convergence.

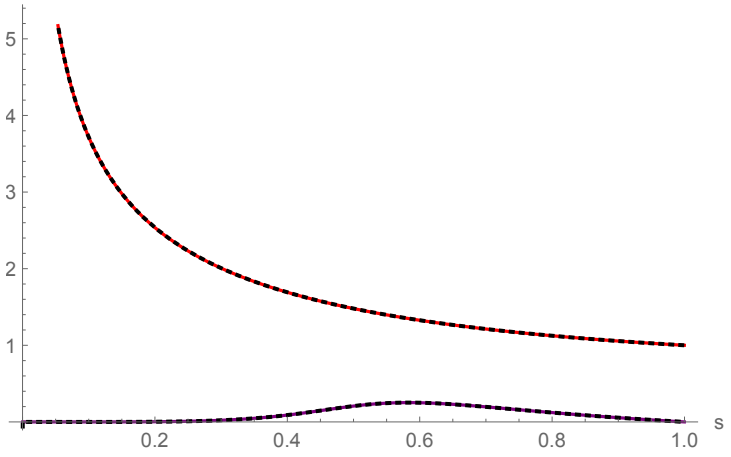

(A)

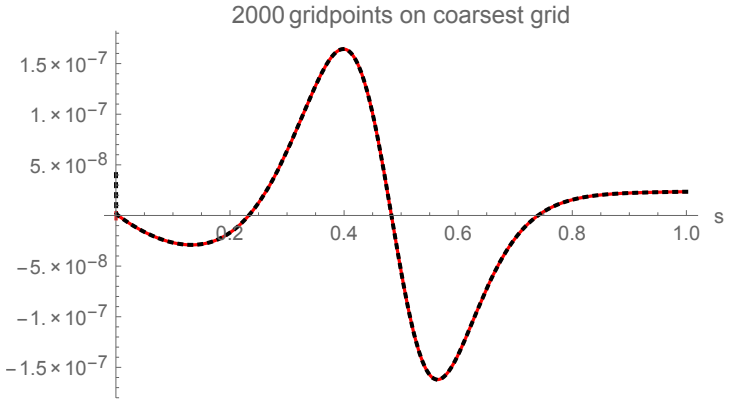

(B)

FIGURE 11. (A) Plot of the numerically obtained deviation $[u]$ (black, dashed) over the corresponding analytical curve (blue, line), and the same for the solution $[\psi]$; (black, dashed) over (red, line). The number of grid points is $n = 2\,000$. A second order self-convergence test is shown in (B). Denoting the interpolations of the deviations with n, $2n$ and $4n$ grid points by u_n, u_{2n} and u_{4n}, we have $u_{2n} - u_n$ in (red, lined) and $4(u_{4n} - u_{2n})$ in (black, dashed).

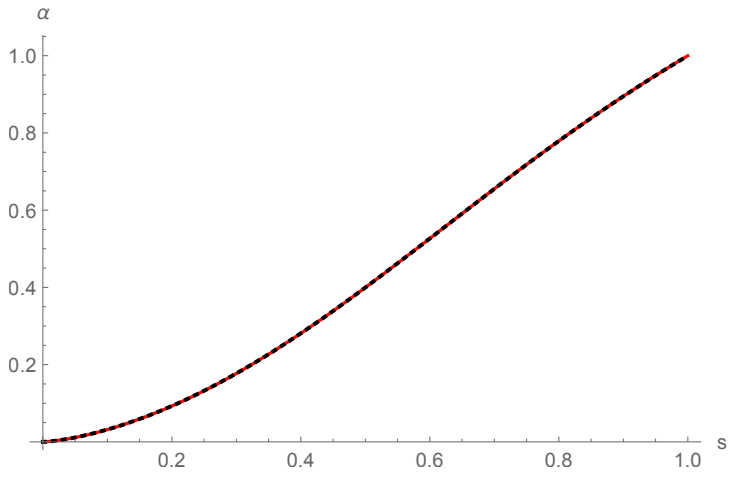

(A)

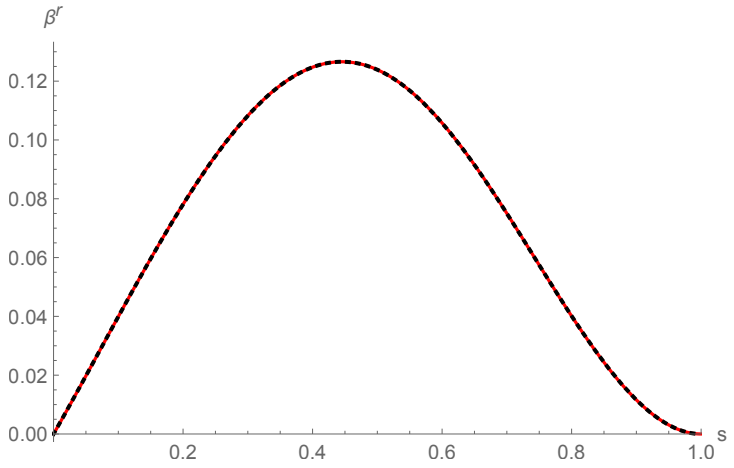

(B)

FIGURE 12. Plots of the Killing lapse (A) and Killing shift (B). The numerical solutions are (black, dashed) over the analytical solutions (red, line). The number of grid points is $n = 2\,000$.

CHAPTER 7

A numerical derivation of maximal extreme Kerr trumpet initial data

In this chapter we solve for the maximal extreme Kerr trumpet in a generalisation of the approached of the previous chapter. Each constraint equation is treated separately. In section 1 we discuss the numerical solver for the conformal metric. The solvers for the Hamiltonian and momentum constraints are discussed in sections 2 and 3. We show convergence to the analytical solution for each of the solvers, and elaborate on work in progress to combine them to solve the coupled system simultaneously.

We will refrain from writing out grid indices here to avoid to overload the notation with both, spatial and grid indices at the same time. Instead we use shorthands, such as $[\beta^\phi]$ to denote the matrix of values of β^ϕ on the numerical grid.

1. Solving for the conformal metric

In section 2 of chapter 5 we outlined our approach to solve for the conformal metric $\bar{\gamma}_{ij}$ and arrived at the equation

$$\begin{aligned} 0 = \psi^{-4}\Big(\alpha\Big(R_{ij} - \frac{\psi^4}{3}\bar{\gamma}_{ij}R\Big) - \Big(D_iD_j\alpha - \frac{\psi^4}{3}\bar{\gamma}_{ij}D_kD^k\alpha\Big)\Big) \\ - 2\alpha\tilde{A}_{ik}\tilde{A}_j{}^k + \bar{D}_i\beta^k\tilde{A}_{kj} + \bar{D}_j\beta^k\tilde{A}_{ki} - \frac{2}{3}\bar{D}_k\beta^k\tilde{A}_{ij} + \beta^k\bar{D}_k\tilde{A}_{ij}. \end{aligned} \tag{59}$$

Further, in section 5 of chapter 5, we discussed that we make an ansatz of the form

metric ansatz with perturbation h

$$\bar{\gamma}_{ij} = \mathrm{diag}[1, r^2, r^2\sin(\theta)^2(1+h)], \tag{69}$$

in which the only deviation from conformal flatness enters through the factor $h(r,\theta)$ to which we will refer to as metric perturbation. We will now perform a transformation into new coordinates $\{s,t\}$ given by

$$r = \frac{s}{1-s} \qquad \text{and} \qquad \theta = \pi t,$$

such that the original domain $[0,\infty)\times[0,\pi]$ is compactified to $[0,1]\times[0,1]$. Plugging then (69) into (59) we arrive at a differential equation for h for each component ij of the equation. Each of these of course must yield the same solution h. We chose the st-component, for which the resulting equation takes the form

equation for h

$$c_0 + c_1 h + c_2\partial_s h + c_3\partial_s\partial_t h + c_4\frac{\partial_s h\partial_t h}{1+h} = 0. \tag{88}$$

The coefficients c_λ generally depend on the quantities ψ, $\bar{\alpha}$, β^ϕ, $\bar{A}_{s\phi}$ and $\bar{A}_{t\phi}$, and on the coordinates s and t directly. However, as stated in the beginning of this chapter, for our first take we provide those quantities from the known analytical solution, so we view the coefficients as functions of the coordinates only for now; ie $c_\lambda(s,t)$. It turns out that c_2 diverges for $s\to 0$ and $s\to 1$ as t^{-1} and $(1-t)^{-1}$ respectively.

To avoid problems caused by that with our numerical solver, we therefore define a new quantity g which is related to h by

$$h = t(1-t)g, \tag{89}$$

and to which we will refer to as the modified metric perturbation. Reformulating (88) as an equation for g we arrive at

$$d_0 + d_1 g + d_2 \partial_s g + d_3 \partial_s \partial_t g + d_4 \frac{\partial_s g \partial_t g}{1 + t(1-t)g} + d_5 \frac{g \partial_s g}{1 + t(1-t)g} = 0, \tag{51}$$

where we again view the coefficients d_λ as coordinate functions $d_\lambda(s,t)$, which are now all regular on the whole domain, including the boundaries.

lienarisation

(51) is clearly nonlinear. Hence, as discussed in section 5 of chapter 4, we solve it by iteratively solving its linearisation for a correction δg:

$$g^{\iota+1} = g^\iota + \delta g^\iota.$$

Here ι represents the iteration index. Therefore, the initial guess or current solution g^ι gets corrected by δg^ι iteratively until a convergence criteria is met. We already worked out the linearisation of (51) in section 5 if chapter 4. It is given by

$$b_0 + b_1 \delta g + b_2 \partial_s \delta g + b_3 \partial_t \delta g + b_4 \partial_s \partial_t \delta g = 0, \tag{52}$$

where the coefficients b_λ, given by (53), now depend on the current solution g and its derivatives, and apart from that are viewed as coordinate functions; ie $b_\lambda[g](s,t)$.

linear solver

We use Mathematica's LinearSolve command using the method Banded to solve the finite difference equation corresponding to (52) at each iteration step. The solution failed to converge using two-sided finite difference derivatives, but converged using one-sided finite difference derivatives. For completeness we mention that we initially attempted to solve (52) by the same successive over-relaxation methods which we already successfully applied to the Hamiltonian and momentum constraints before; cf sections 2 and 3. This however did not succeed, and we assumed that the method may not be applicable to this problem. In this context we note that evaluating the coefficients b_λ for the analytical solution of g on the domain, we find that (52) is hyperbolic, cf [42, p 26], as opposed to all our other constraint equations which are elliptic. Relaxation methods however are usually applied to elliptic problems.

boundary conditions

We turn now to the boundary conditions: For the correction δg we can choose a Dirichlet condition of value 0 at all boundaries, since it should converge to zero. The boundary conditions for g enter in the finite difference evaluation of the coefficients b_λ at each iteration step. For our first take in tackling the problem, we will make some use of the analytical solution here. A plot of the analytically given metric perturbation h, cf (70), is shown in figure 12. The modified metric perturbation g is respectively given by a multiplication of h by $t(1-t)$; cf (89). For the angular boundaries $t = 0$ and $t = 1$ we could use symmetric boundary conditions, eg $g(s,-\Delta t) = g(s,\Delta t)$, since the axial symmetry clearly dictates all quantities to be symmetric with respect to a transition through the poles. We however use Dirichlet conditions of value 0 in our current version of the solver. Because of asymptotic flatness we would expect the metric perturbation to vanish at infinity. Hence we can also choose a Dirichlet condition of value 0 at $s = 1$. The only nontrivial boundary condition is the lower boundary condition, ie at $s = 0$. In our first attempt we simply make use of the analytical value given by (70), and implement it as Dirichlet condition. Taking an extreme Kerr black hole of mass $m = 1$, our

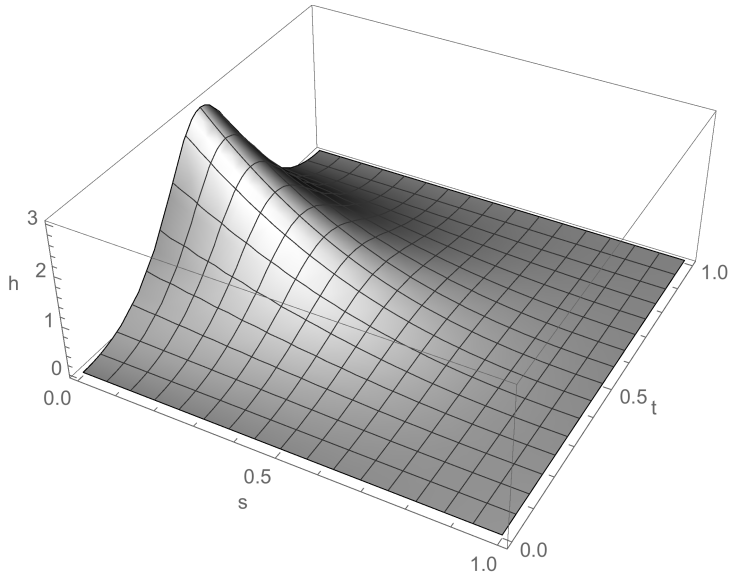

FIGURE 12. Plot of the metric perturbation h for an extreme Kerr black hole of mass $m = 1$, as analytically given by (70).

chosen boundary conditions are then summarised by

$$h(0,t) = -1 + \frac{16}{(3+\cos(2\pi t))^2}, \qquad h(s,0) = 0,$$
$$h(1,t) = 0, \qquad h(s,1) = 0.$$

The corresponding lower boundary condition for the modified metric perturbation g is respectively given using (89). We will elaborate at the end of this chapter on our strategy of how to come up with a lower boundary condition without making direct use of the analytical solution.

results

We continue with the choice of an extreme Kerr black hole of mass $m = 1$. Running the solver on a 32×32 grid, it hits the convergence criterion after 352 iterations, the latter being that the L^2 norm of the residual of the finite difference equation, ie of the coefficient $[b_0]$, divided by the number of grid-points gets smaller than 10^{-8}:

$$\frac{|||[b_0]|||}{n} < 10^{-8}.$$

The resulting numerical solution $[h]$ is shown in figure 13. Figure 14 shows the error of the numerical to the analytical solution, and figure 15 the final correction $[\delta h] = [t(1-t)\delta g]$ which is obtained at the last iteration step.

future work

We conclude this section with an outlook on future work on this solver. First, so far we provided our solver with the analytic quantities ψ, $\bar{\alpha}$, β^ϕ, $\bar{A}_{s\phi}$ and $\bar{A}_{t\phi}$, which enter the coefficients b_λ. Solving the full system of constraints these would have to be provided from the other solvers. Second, as mentioned earlier in this section, so far we provide the lower boundary condition for h, or g respectively, from the analytical solution as well. One idea to avoid that would be to reformulate the differential equation (88), or (51) respectively, as an equation for a quantity (sh), or (sg), which would meet a trivial Dirichlet condition of value 0 at the lower boundary. Finally, our solver currently does not converge for arbitrary grid resolutions, which in particular prevents us from performing a proper convergence test for now. At the time of writing we did not yet have time for a proper look into this problem.

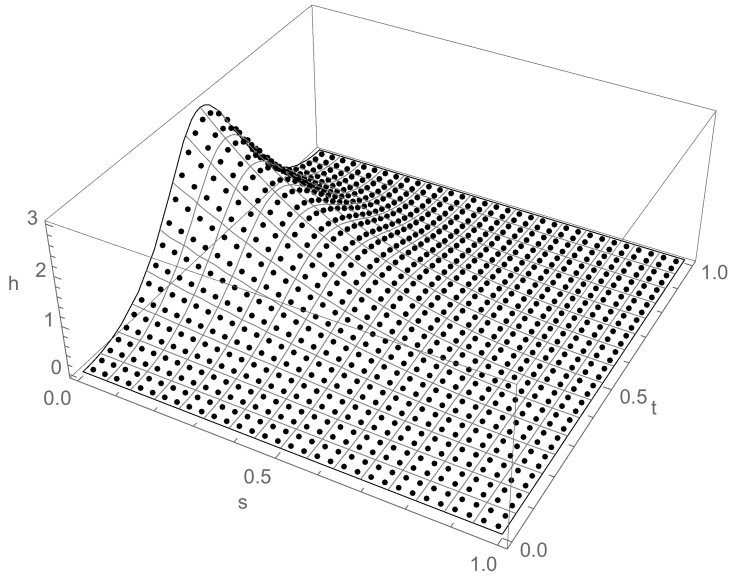

FIGURE 13. Plot of the numerical (dots) together with the analytical solution (mesh) of h for an extreme Kerr black hole of mass $m = 1$. The grid size is 32×32 and the convergence criterion is $|||[b_0]||| < 10^{-8}$.

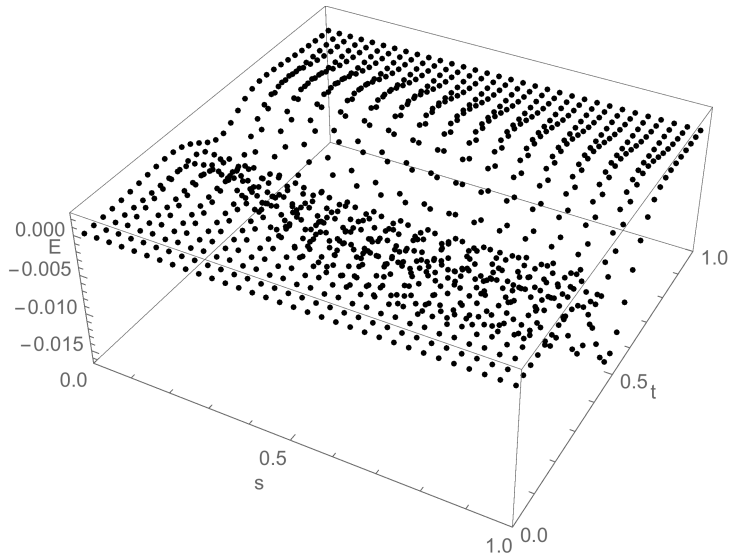

FIGURE 14. Plot of the error of $[h]$, ie the analytical minus the numerical solution.

2. Hamiltonian constraint

In section 1 of chapter 5 we reduced the Hamiltonian constraint for our problem already to the form

$$\bar{\gamma}^{ij}\bar{D}_i\bar{D}_j\psi - \frac{1}{8}\psi\bar{R} + \frac{1}{8}\psi^{-7}\bar{A}_{ij}\bar{A}^{ij} = 0. \tag{55}$$

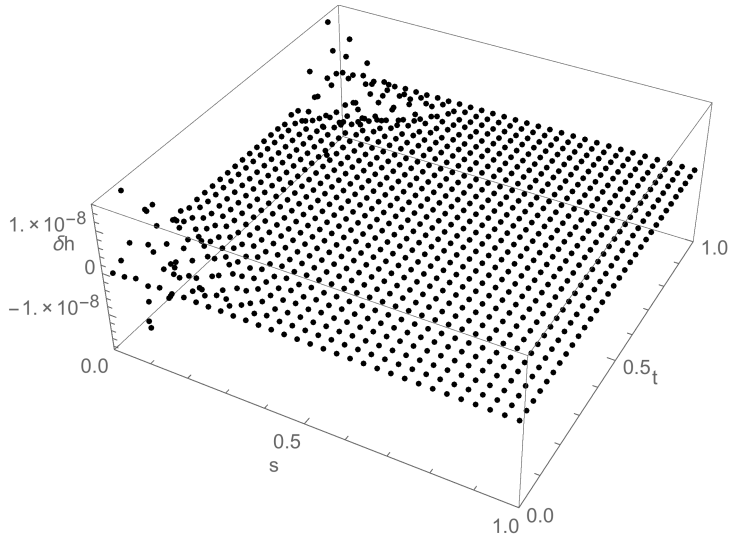

FIGURE 15. Plot of the correction $[\delta h] = [t(1-t)\delta g]$ after the final iteration.

This is to be solved for the conformal factor ψ. As with the solver for the metric perturbation discussed in section 1, we will as well provide all the other geometric quantities in the equation analytically in our first take to solve (55). In this case these are $\bar{A}_{ij}\bar{A}^{ij}$ and h; cf section 5 of chapter 5. Note that $\bar{R}$ is constructed from h. Many of the steps to solve this equation are analogous to the ones performed in section 1. Hence we will not go into as much detail on these here, but rather focus on the differences and results.

solution ansatz

As we have already seen with trumpet solutions, and can see from the analytic solution (74), that ψ goes as $1/\sqrt{r}$ as r goes to 0. To deal with this divergence in our solver we proceed in the same manner as in the case of the Schwarzschild Hamiltonian constraint in chapter 6, and split ψ up into an analytical ansatz ψ_0, which carries the divergence, and into a regular deviation u, which we solve for;

$$\psi = \psi_0 + u. \tag{90}$$

We choose

$$\psi_0 = w_1(r)\sqrt{\frac{M}{|r|}}(1+\cos(\theta)^2)^{1/4} + w_2(r)\Big(1+\frac{M}{2r}\Big). \tag{91}$$

The two weight functions $w_1(r) = \frac{1}{1+r^4}$ and $w_2(r) = \frac{r^4}{1+r^4}$ are mediating between the divergent first term for small r and the to asymptotical flatness corresponding second term as r goes to ∞. As already discussed in section 3 of chapter 5, the $\sqrt{M/r}$ factor of the first term in (91) can be guessed straightforwardly, while its angular dependence $(1+\cos(\theta)^2)^{1/4}$ cannot simply be guessed. In our first take we will therefore prescribe it from the analytical solution (74). A strategy to solve for it separately has already been discussed in section 3 of chapter 5; cf the discussion surrounding (60). The absolute value under the square root in (91) merely serves the purpose that ψ_0 can also be evaluated at the ghost points off the grid of our numerical solver.

linearisation

With (90), the Hamiltonian constraint (55) represents now an elliptic equation for the deviation u. Since it is nonlinear we solve it by linearisation and iteration

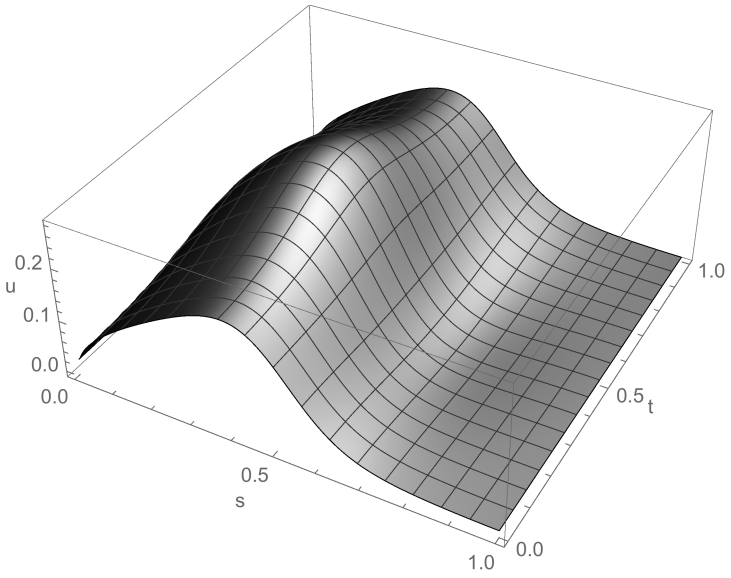

FIGURE 16. Plot of the interpolation of the numerical solution $[u]$ produced by our solver. The grid size is 320×160. The breaking conditions are set to $\max|\omega[res]| < 10^{-8}$ or 60 000 iterations and $\max|[\delta u]| < 10^{-8}$ respectively.

in the same way as in section 1, following the scheme

$$u^{\iota+1} = u^{\iota} + \delta u^{\iota}, \tag{92}$$

where the initial guess or current solution u^{ι} is updated by a correction δu^{ι} which is solved for at each iteration step ι.

linear solver, initial guess and boundary conditions

To solve the linearised equation we use our own finite difference successive over-relaxation (SOR) solver, which we coded in Mathematica. Its SOR parameter ω is set to 1, cf section 4 of chapter 4. We start with an initial guess of $u^1 = 0$. Given that the ansatz (91) has the correct behaviour towards $r = 0$ and $r = \infty$, we can set Dirichlet conditions of value 0 for both u and δu at both the lower and the upper boundaries. Expressed in the variables s and t that is

$$\begin{aligned} u(0,t) &= 0, & u(1,t) &= 0, \\ \delta u(0,t) &= 0, & \delta u(1,t) &= 0. \end{aligned}$$

For the angular boundaries we set symmetric conditions:

$$\begin{aligned} u(s,\Delta t) &= u(s,-\Delta t), & u(s,1+\Delta t) &= u(s,1-\Delta t), \\ \delta u(s,\Delta t) &= u(s,-\Delta t), & \delta u(s,1+\Delta t) &= \delta u(s,1-\Delta t). \end{aligned}$$

results

Figure 16 shows the interpolation of the solution $[u]$ produced by our solver on a 320×160 grid for an extreme Kerr black hole of mass $m = 1$. The corresponding error is shown in figure 17. As breaking condition for the linear solver we set

$$\max|\omega[res]| < 10^{-8} \quad \text{or} \quad 60\,000 \text{ iterations},$$

where ω denotes the SOR parameter and $[res]$ the SOR residual matrix; cf section 4 of chapter 4. Consequently, as breaking condition for the iterative process (92) we set

$$\max|[\delta u]| < 10^{-8}.$$

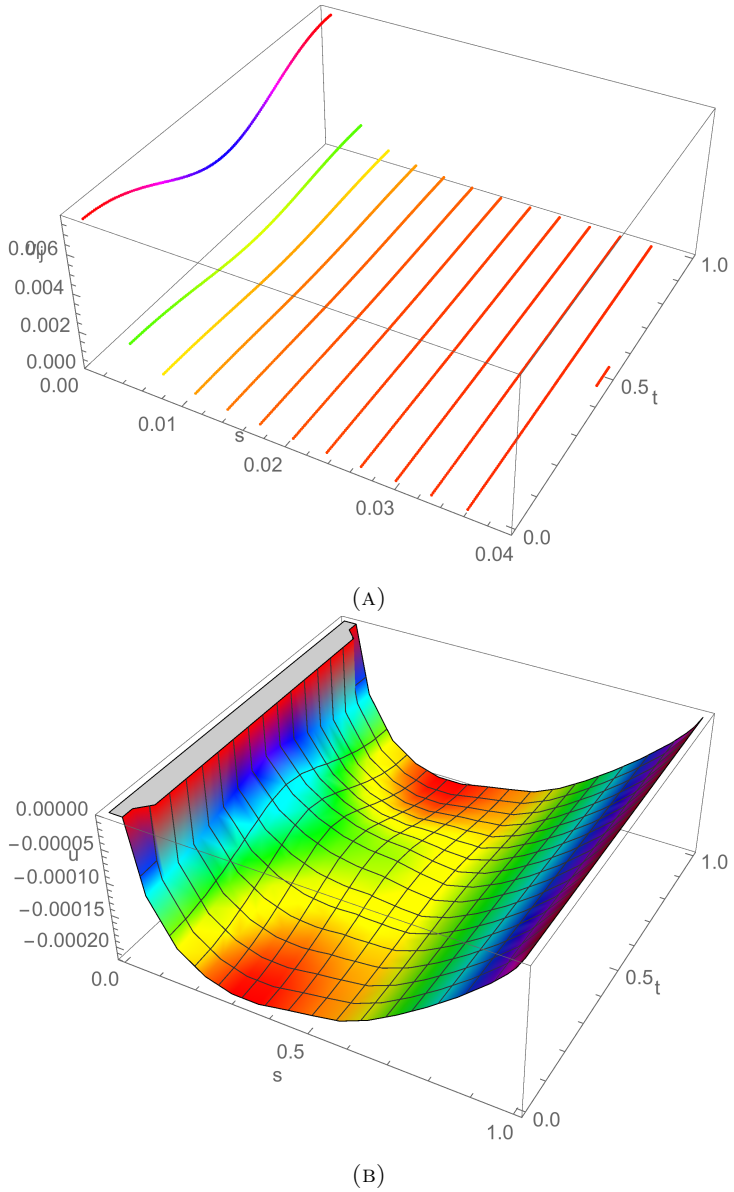

FIGURE 17. Plot of the error of $[u]$. The positive error is shown in (A), while (B) shows the interpolation of the negative error. Note that the s-range is restricted to $[0, 0.04]$ in the former case.

convergence

Finally, we demonstrate convergence at hand of the the line $\theta = \pi/2$, or $t = 0.5$. Figure 18a shows the errors of the grid-lines closest to $\theta = \pi/2$ for five different solutions of grid-sizes from 20×10 to 320×160. Figure 18b shows the same plot where however the solutions are scaled for a second order convergence test. The test shows a clean overlap for the lower three resolutions. The curve for the 160×80 resolution is slightly off, while the error of the 320×160 solution changes somewhat in character. We assume that the chosen tolerance of 10^{-8} is too high to yield the optimal accuracy with this resolution; cf section 2 of chapter 4.

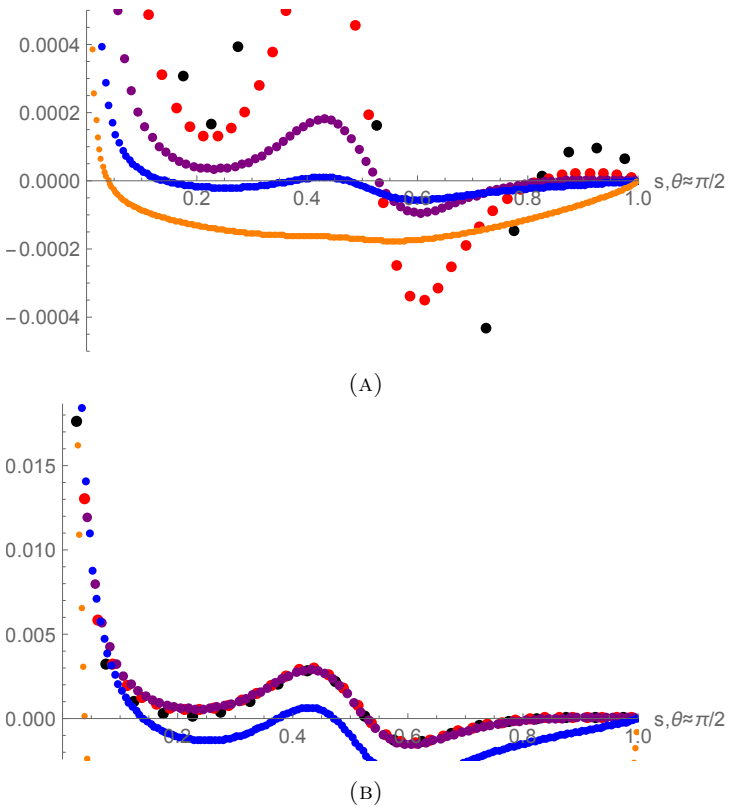

FIGURE 18. Convergence test for $t \approx 0.5$, ie $\theta \approx \pi/2$. (A) shows the errors of $[u]$ for resolutions 20×10 (black), 40×20 (red), 80×40 (purple), 160×80 (blue) and 320×160 (orange). In (B) these are multiplied by 1, 4, 16, 64 and 256 respectively, to test for second order convergence.

3. Momentum constraint

In section 1 of chapter 5 we reduced the momentum constraint for our problem already to the form

$$(\bar{\Delta}_{\bar{L}} V)^i - (\bar{L}V)^{ij}\bar{D}_j \ln\bar{\sigma} = 0. \tag{56}$$

use conformal thin sandwich approach

This elliptic equation is to be solved for the vector potential V^i. In our first take we use the conformal thin sandwich approach which we discussed in section 5 of chapter 2. This means we prescribe the weight function as $\bar{\sigma} = 2\bar{\alpha}$, taking $\bar{\alpha}$ from (65), and consequently solve (56) for the shift β^i, of which the only non-vanishing component is that in ϕ-direction; cf (66). We also prescribe the metric perturbation h from (70).

To solve the momentum constraint we apply the same techniques as for the Hamiltonian constraint in section 2. There are however two main differences. First, (56) is linear. Hence we do not need to linearise and iterate as in (92), but can directly solve the constraint with our finite difference successive over-relaxation solver. Second, the solution β^ϕ is regular on the domain, including the boundaries. Hence we do not need an ansatz of the form (90).

boundary conditions

As boundary conditions we choose the following:

$$\beta^\phi(0,t) = -1/2m, \qquad \beta^\phi(s,-\Delta t) = \beta^\phi(s,\Delta t),$$
$$\beta^\phi(1,t) = 0, \qquad \beta^\phi(s,1-\Delta t) = \beta^\phi(s,1+\Delta t).$$

The angular boundary conditions are chosen to be symmetric. The upper boundary condition, ie for $s = 1$, is motivated by asymptotic flatness. Finally, the only non-trivial boundary condition is again the lower boundary condition, ie for $s = 0$. In our first approach we use our knowledge of the analytical solution here, and simply implement the known value as Dirichlet condition. We will discuss work in progress to motivate a lower boundary condition without direct use of the analytical solution at the end of this section.

convergence criterion, SOR parameter and results

As convergence criterion we set that

$$\max|\omega[res]| < 10^{-8},$$

and we set the SOR parameter to $\omega = 0.9$. For a grid-size of 160×80 our solver passes this criterion after 58 178 iterations. Plots of the obtained solution $[\beta^\phi]$ and of its error are shown in figure 19. A convergence test at hand of the line $t = 1$, or $\theta = \pi/2$, is shown in figure 20. The curves overlap nicely for the lower two resolutions, while they are off for the higher two resolutions. Again we assume that in the latter cases the limiting factor is the chosen tolerance; cf section 2 of chapter 4.

calculation of $\bar{A}_{ij}$ and $\bar{A}_{ij}\bar{A}^{ij}$

In the context of solving the whole system of constraints (55), (56) and (59), the momentum constraint also serves the purpose of providing the extrinsic curvature $\bar{A}_{ij}$ and in particular the quantity $\bar{A}_{ij}\bar{A}^{ij}$ for the other equations, which can be calculated by (10), with $\bar{M}^{ij} = 0$, and (62) respectively. In our current case where we use the conformal thin sandwich approach this is

$$\bar{A}^{ij} = \frac{1}{2\bar{\alpha}}(\bar{L}\beta)^{ij} \qquad \text{and} \qquad \bar{A}_{ij}\bar{A}^{ij} = \frac{1}{(2\bar{\alpha})^2}(\bar{L}\beta)_{ij}(\bar{L}\beta)^{ij}$$

respectively. Figure 21 shows the quantity $r^6\bar{A}_{ij}\bar{A}^{ij}$ calculated from our solution with 160×80 grid points, as well as its error to the analytical value.

We conclude this section with a discussion on work in progress and future work on this solver. In the preceding part of this section we used the conformal thin sandwich decomposition, where $\bar{\sigma} = 2\bar{\alpha}$ and $V^i = \beta^i$. We were able to prescribe $\bar{\alpha}$, the killing lapse of the stationary extreme Kerr trumpet foliation, since this foliation is readily given by the Kerr solution in quasi-isotropic coordinates.; cf section 5 of chapter 5. This is however not the case for slow Kerr, for which the quasi-isotropic solution represents a wormhole foliation. In our future work on the maximal slow Kerr trumpet we will therefore not be able to prescribe the killing lapse. We will instead have to work in the weighted transverse decomposition and choose a weight function $\bar{\sigma}$ and solve the momentum constraint for a vector potential V^i. As discussed in section 3 of chapter 5 the challenge lies in the need to find a lower boundary condition for V^i, and we outlined our strategy to use the imposition (61) to do so there. We could already successfully apply this strategy in the case of the maximal Schwarzschild trumpet in chapter 6. In the following we present our work in progress for extreme Kerr.

First, because of axial symmetry we can choose both the weight function $\bar{\sigma}$ and the vector potential V^i to depend on the coordinates s and t only, ie to be independent of ϕ. Second, we impose the vector potential which we solve for to have a non-trivial ϕ-component only, ie $[V^i] = [0, 0, V^\phi]^{\mathrm{T}}$. Finally, to yield a simple lower boundary condition, we impose that V^ϕ shall be independent of t at the lower

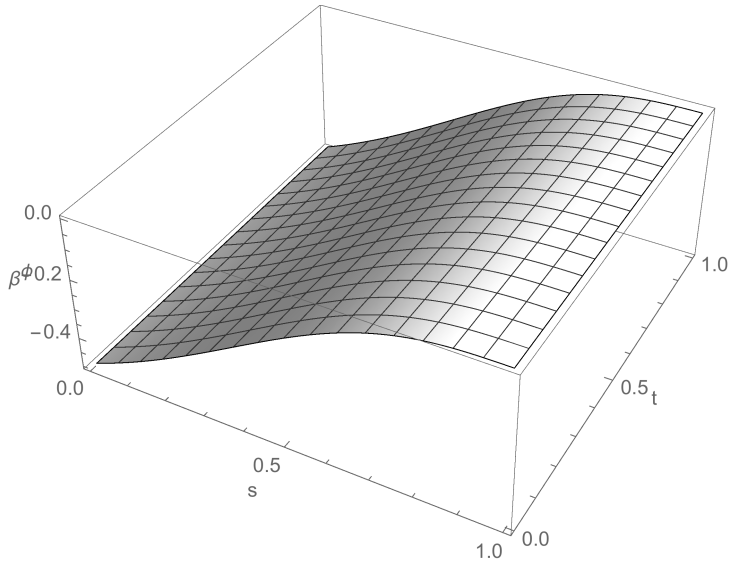

(A)

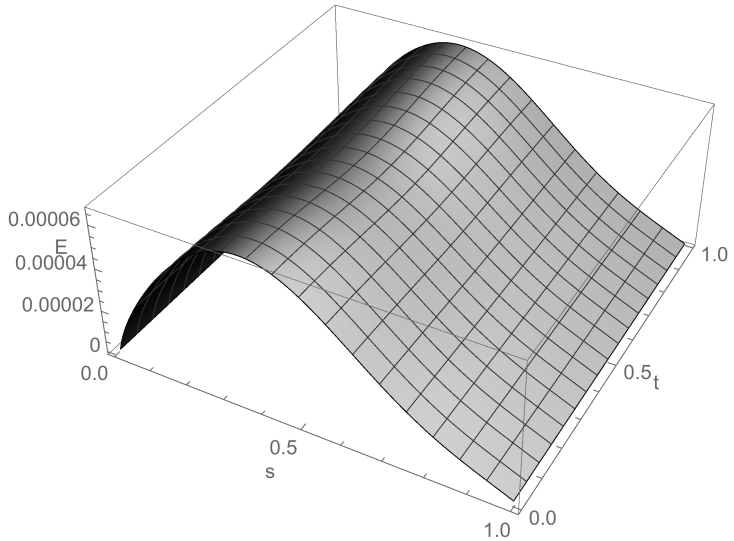

(B)

FIGURE 19. Plot of the interpolation of the solution $[\beta^\phi]$ (A) together with its error (B). The grid size is 160×80. The convergence criterion is $\max|\omega[res]| < 10^{-8}$.

boundary, ie

$$\partial_t V^\phi(0,t) = 0.$$

Plugging this into the expression $(\bar{L}V)_{ij}(\bar{L}V)^{ij}$ and developing it in a series around $s = 0$ we find that

$$(\bar{L}V)_{ij}(\bar{L}V)^{ij} \overset{s\to0}{\simeq} 32\frac{\sin(\pi t)^2}{(3+\cos(2\pi t))^2}\partial_s V^\phi(0,t)^2 s^2,$$

and multiplying this by $1/\bar{\sigma}^2$ we get from (62) that

$$\bar{A}_{ij}\bar{A}^{ij} \overset{s\to0}{\simeq} 32\frac{\partial_s V^\phi(0,t)^2}{\bar{\sigma}(s,t)^2}\frac{\sin(\pi t)^2}{(3+\cos(2\pi t))^2}s^2, \tag{93}$$

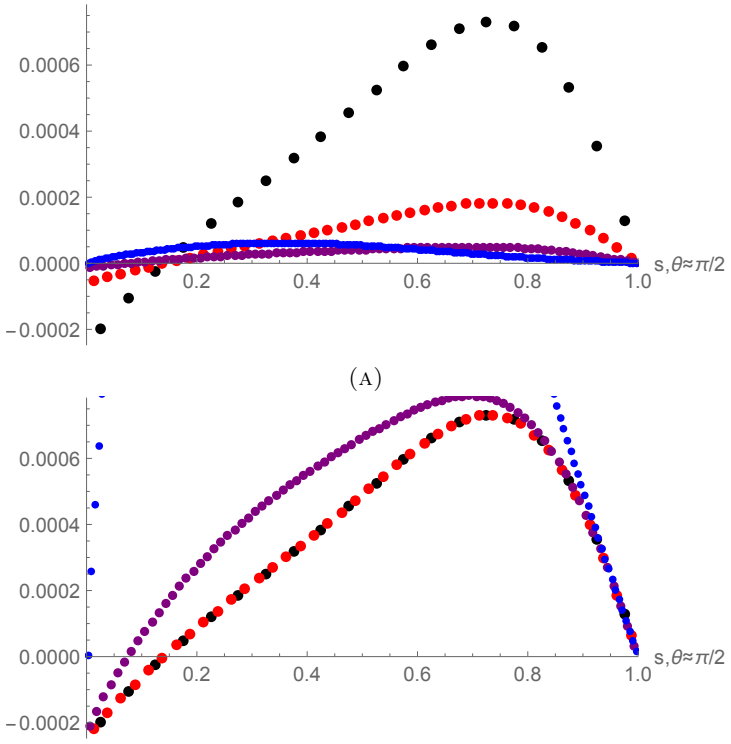

(A)

(B)

FIGURE 20. Convergence test for $t \approx 0.5$, ie $\theta \approx \pi/2$. (A) shows the errors of $[\beta^\phi]$ for resolutions 20×10 (black), 40×20 (red), 80×40 (purple) and 160×80 (blue). In (B) these are multiplied by 1, 4, 16 and 64 respectively, to test for second order convergence.

to leading order in s. On the other hand, we said that we impose (61), or equivalently for extreme Kerr, that we allow ourselves to use (72), ie

$$\bar{A}_{ij}\bar{A}^{ij} \overset{s\to 0}{\simeq} \frac{2m^4}{s^6}\sin(\pi t)^2. \tag{94}$$

Equating (93) and (94) we arrive at the relation

$$1 = \frac{4}{m^2}\frac{\partial_s V^\phi(0,t)}{\bar{\sigma}(s,t)}\frac{s^4}{3+\cos(2\pi t)} \qquad \text{for small } s. \tag{95}$$

To convince ourselves of the validity of this relation we check if it holds for the gauge functions (65) and (66). In a series around $s = 0$ we find

$$2\bar{\alpha} \overset{s\to 0}{\simeq} \frac{2}{m^4}\frac{s^4}{3+\cos(2\pi t)} \qquad \text{and} \qquad \beta^\phi \overset{s\to 0}{\simeq} -\frac{1}{2m} + \frac{1}{2m^2}s.$$

From the latter we see that $\partial_s\beta^\phi(0,t) = 1/2m^2$. Plugging this and the just quoted behaviour of $2\bar{\alpha}$ into (95), we see that the relation is indeed satisfied.

We can now use relation (95) to find a lower boundary condition for V^ϕ in accordance with a chosen $\bar{\sigma}$. We could for instance choose

$$\bar{\sigma} = \frac{4}{m^4}\frac{s^4}{3+\cos(2\pi t)},$$

with which (95) yields

$$\partial_s V^\phi(0,t) = 1/m^2,$$

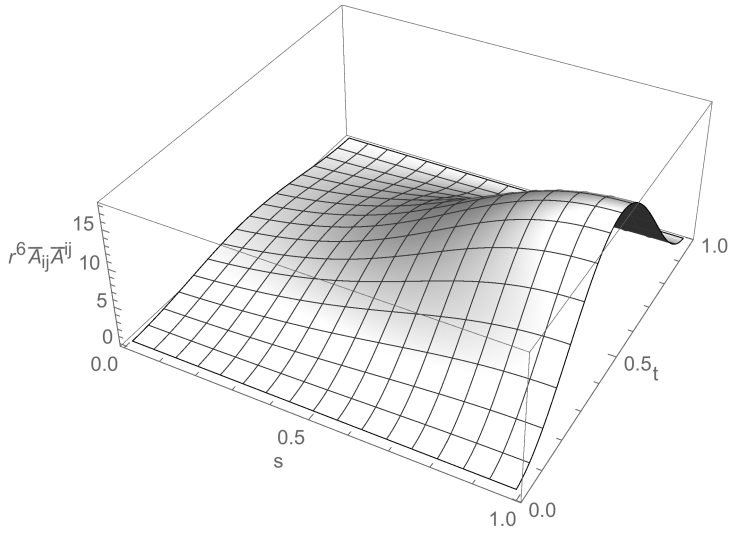

(A)

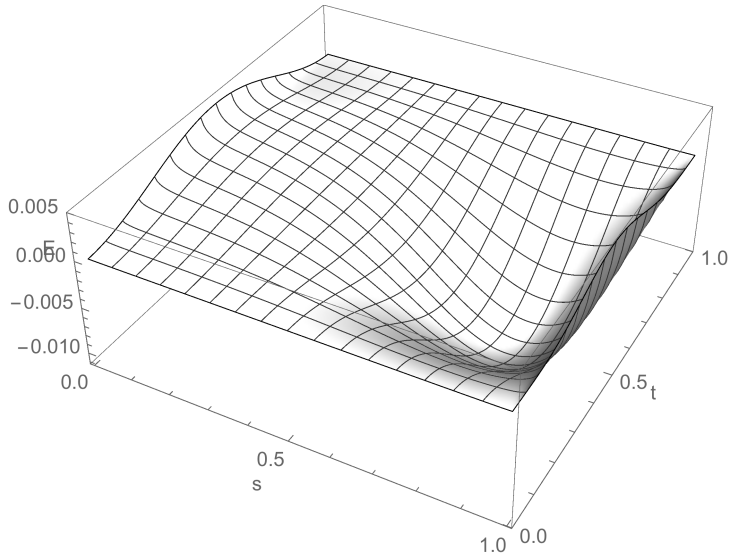

(B)

FIGURE 21. Plot of the interpolation of $[r^6\bar{A}_{ij}\bar{A}^{ij}]$ (A), as calculated from our numerical solution $[\beta^\phi]$, together with its error (B). The grid size is 160×80.

ie a Neumann condition of value $1/m^2$ at the lower boundary. We used this choice of $\bar{\sigma}$ and the corresponding lower boundary condition in our solver, as well as other combinations. While the solutions would generally converge, unfortunately the quantity $r^6\bar{A}_{ij}\bar{A}^{ij}$ would not yield the correct value away from $s = 0$. At the time of writing we are not sure why this is the case.

Bibliography

[1] Alcubierre M: Introduction to 3+1 Numerical Relativity; *International Series of Monographs in Physics – 104*; Oxford University Press (2008).
ISBN: 978-0-19-920567-7
Cited on page 5, 7, 8, 9, 11, 14, 15, 16, 17, 32

[2] Alcubierre M et al: Gauge conditions for long-term numerical black hole evolutions without excision; *Physical Review D (Volume 67, Issue 8)*, American Physical Society (2003).
DOI: 10.1103/PhysRevD.67.084023
Preprint: arXiv:gr-qc/9412071v2
Cited on page 15, 16

[3] Alcubierre M et al: Black hole excision for dynamic black holes; *Physical Review D (Volume 64, Issue 6)*, American Physical Society (2001).
DOI: 10.1103/PhysRevD.64.061501
Preprint: arXiv:gr-qc/0104020v2
Cited on page 16

[4] Arnowitt R et al: The dynamics of general relativity; *Witten L editor, Gravitation: An introduction to current research (chapter 7, pages 227-265)*, John Wiley & Sons (1962).
DOI: 10.1103/PhysRevD.64.061501
Republication DOI: 10.1007/s10714-008-0661-1
Preprint: arXiv:gr-qc/0405109v1
Cited on page 5, 8

[5] Baker JG et al: Gravitational-Wave Extraction from an Inspiraling Configuration of Merging Black Holes; *Physical Review D (Volume 96, Issue 11)*, American Physical Society (2006).
DOI: 10.1103/PhysRevLett.96.111102
Preprint: arXiv:gr-qc/0511103v1
Cited on page 13, 16

[6] Baumgarte TW: Puncture black hole initial data in the conformal thin-sandwich formalism; *Classical and Quantum Gravity (Volume 28, Number 21)*, Institute of Physics Publishing (2011).
DOI: 10.1088/0264-9381/28/21/215003
Preprint: arXiv:1108.3550v1 [gr-qc]
Cited on page 19, 34

[7] Baumgarte TW and Naculich SG: Analytical Representation of a Black Hole Puncture Solution; *Physical Review D (Volume 75, Issue 6)*, American Physical Society (2007).
DOI: 10.1103/PhysRevD.75.067502
Preprint: arXiv:gr-qc/0701037v1
Cited on page 19

[8] Baumgarte TW and Shapiro SL: Numerical Relativity: Solving Einstein's Equations on the Computer, Cambridge University Press (2010).
ISBN: 978-0-521-51407-1
Cited on page 5, 7, 11, 15, 26

[9] Beig R and Murchadha NÓ: Late time behavior of the maximal slicing of the Schwarzschild black hole; *Physical Review D (Volume 57, Issue 5)*, American Physical Society (1998).
DOI: 10.1103/PhysRevD.57.4728
Preprint: arXiv:gr-qc/9706046v1
Cited on page 17

[10] Beig R: The maximal slicing of a Schwarzschild black hole; *Annalen der Physik (Volume 11, Issue 5)*, Wiley-VCH (2000).
Preprint: arXiv:gr-qc/0005078v1
Cited on page 17

[11] Bona C et al: New Formalism for Numerical Relativity; *Physical Review Letters (Volume 75, Issue 4)*, American Physical Society (1995).
DOI: 10.1103/PhysRevLett.75.600
Preprint: arXiv:gr-qc/9412071v2
Cited on page 16, 31

[12] Bowen JM and York JW: Time-asymmetric initial data for black holes and black-hole collisions; *Physical Review D (Volume 21, Issue 8)*, American Physical Society (1980).
DOI: 10.1103/PhysRevD.21.2047
Cited on page 15

[13] Brandt SR and Brügmann: A Simple Construction of Initial Data for Multiple Black Holes; *Physical Review Letters (Volume 78, Issue 19)*, (1997).
DOI: 10.1103/PhysRevLett.78.3606
Preprint: arXiv:gr-qc/9703066v2
Cited on page 16

[14] Brandt SR and Seidel E: Evolution of distorted rotating black holes. III. Initial data; *Physical Review D (Volume 54, Issue 2)*, American Physical Society (1996).
DOI: 10.1103/PhysRevD.54.1403
Preprint: arXiv:gr-qc/9601010v1
Cited on page 35

[15] Brill DR and Lindquist RW: Interaction Energy in Geometrostatics; *Physical Review (Volume 131, Issue 1)*, American Physical Society (1963).
DOI: 10.1103/PhysRev.131.471
Cited on page 15

[16] Brown JD: Puncture evolution of Schwarzschild black holes; *Physical Review D (Volume 77, Issue 4)*, American Physical Society (2008).
DOI: 10.1103/PhysRevD.77.044018
Preprint: arXiv:0705.1359v3 [gr-qc]
Cited on page 16

[17] Campanelli M et al: Accurate Evolutions of Orbiting Black-Hole Binaries without Excision; *Physical Review D (Volume 96, Issue 11)*, American Physical Society (2006).
DOI: 10.1103/PhysRevLett.96.111101
Preprint: arXiv:gr-qc/0511048v2
Cited on page 13, 16

[18] Cook GB and York JW: Apparent horizons for boosted or spinning black holes; *Physical Review D (Volume 41, Issue 4)*, American Physical Society (1990).
DOI: 10.1103/PhysRevD.41.1077
Cited on page 16

[19] Dain S and Gabach Clément ME: Extreme Bowen-York initial data; *Classical and Quantum Gravity (Volume 26, Number 3)*, Institute of Physics Publishing (2009).
DOI: 10.1088/0264-9381/26/3/035020
Preprint: arXiv:0806.2180v1 [gr-qc]
Cited on page 19, 34

[20] Dennison KA and Baumgarte TW: A simple family of analytical trumpet slices of the Schwarzschild spacetime; *Classical and Quantum Gravity (Volume 31, Number 11)*, Institute of Physics Publishing (2014).
DOI: 10.1088/0264-9381/31/11/117001
Preprint: arXiv:1403.5484v1 [gr-qc]
Cited on page 19

[21] Dennison KA et al: Trumpet Slices in Kerr Spacetimes; *Physical Review Letters (Volume 113, Issue 26)*, American Physical Society (2014).

DOI: 10.1103/PhysRevLett.113.261101
Preprint: arXiv:1409.1887v2 [gr-qc]
Cited on page 17, 19

[22] Estabrook F et al: Maximally Slicing a Black Hole; *Physical Review D (Volume 7, Issue 10)*, American Physical Society (1973).
DOI: 10.1103/PhysRevD.7.2814
Cited on page 17

[23] Gabach Clément ME: Conformally flat black hole initial data with one cylindrical end; *Classical and Quantum Gravity (Volume 27, Number 12)*, Institute of Physics Publishing (2010).
DOI: 10.1088/0264-9381/27/12/125010
Preprint: arXiv:0911.0258v2 [gr-qc]
Cited on page 19, 34

[24] Hannam M et al: Wormholes and trumpets: Schwarzschild spacetime for the moving-puncture generation; *Physical Review D (Volume 78, Issue 6)*, American Physical Society (2007).
DOI: 10.1103/PhysRevD.78.064020
Preprint: arXiv:0804.0628v2 [gr-qc]
Cited on page 14, 17, 18, 19

[25] Hannam M et al: Geometry and Regularity of Moving Punctures; *Physical Review D (Volume 99, Issue 24)*, American Physical Society (2007).
DOI: 10.1103/PhysRevLett.99.241102
Preprint: arXiv:gr-qc/0606099v2
Cited on page 16

[26] Hannam M et al: Where do moving punctures go?; *Journal of Physics: Conference Series (Volume 66)*, Institute of Physics Publishing (2007).
DOI: 10.1088/1742-6596/66/1/012047
Preprint: arXiv:gr-qc/0612097v3
Cited on page 18, 19, 36, 43

[27] Hannam M et al: Bowen-York trumpet data and black-hole simulations; *Physical Review D (Volume 80, Issue 12)*, American Physical Society (2009).
DOI: 10.1103/PhysRevD.80.124007
Preprint: arXiv:0908.1063v4 [gr-qc]
Cited on page 19, 33, 34, 43

[28] Hannam M et al: Beyond the Bowen-York extrinsic curvature for spinning black holes; *Classical and Quantum Gravity (Volume 24, Number 12)*, Institute of Physics Publishing (2006).
DOI: 10.1088/0264-9381/24/12/S02
Preprint: arXiv:gr-qc/0612001v2
Cited on page 16

[29] Hartle JB: Gravity: An Introduction to Einstein's General Relativity, Addison Wesley (2003).
ISBN: 0-8053-8662-9
Cited on pages 5

[30] Immerman JD and Baumgarte TW: Trumpet-puncture initial data for black holes; *Physical Review D (Volume 80, Issue 6)*, American Physical Society (2009).
DOI: 10.1103/PhysRevD.80.061501
Preprint: arXiv:0908.0337v2 [qr-qc]
Cited on page 19, 34

[31] Kiusalaas J: Numerical Methods in Engineering with Python 3, Cambridge University Press (2013).
ISBN: 978-1-107-03385-6
Additional resources: www.cambridge.org/kiusalaaspython
Cited on page 21, 23, 25

[32] Laguna P: Conformal-thin-sandwich initial data for a single boosted or spinning black hole puncture; *Physical Review D (Volume 69, Issue 10)*, American Physical Society (2004).
DOI: 10.1103/PhysRevD.69.104020

Preprint: arXiv:gr-qc/0310073v1
Cited on page 33

[33] Malec E and Murchadha NÓ: Constant mean curvature slices in the extended Schwarzschild solution and the collapse of the lapse; *Physical Review D (Volume 68, Issue 12)*, American Physical Society (2003).
DOI: 10.1103/PhysRevD.68.124019
Preprint: arXiv:gr-qc/0307046v1
Cited on page 17

[34] Misner CW et al: Gravitation, W. H. Freeman and Company (1973).
ISBN: 0-7167-0344-0
Cited on pages 5

[35] Pfeiffer HP and York JW: Extrinsic curvature and the Einstein constraints; *Physical Review D (Volume 67, Issue 4)*, American Physical Society (2003).
DOI: 10.1103/PhysRevD.67.044022
Preprint: arXiv:gr-qc/0207095v2
Cited on page 9

[36] Press WH et al: Numerical Recipes: The Art of Scientific Computing - Third Edition, Cambridge University Press (2007).
ISBN: 978-0-521-88068-8
Additional resources: www.nr.com
Cited on page 21, 25, 26

[37] Pretorius F: Evolution of Binary Black-Hole Spacetimes; *Physical Review Letters (Volume 95, Issue 12)*, American Physical Society (2005).
DOI: 10.1103/PhysRevLett.95.121101
Preprint: arXiv:gr-qc/0507014
Cited on page 13

[38] Reimann B and Brügmann B: Maximal slicing for puncture evolutions of Schwarzschild and Reissner-Nordström black holes; *Physical Review D (Volume 69, Issue 4)*, American Physical Society(2004).
DOI: 10.1103/PhysRevD.69.044006
Preprint: arXiv:gr-qc/0307036v2
Cited on page 16

[39] Ruchlin I et al: Puncture initial data for black-hole binaries with high spins and high boosts; *Physical Review D (Volume 95, Issue 2)*, American Physical Society (2017).
DOI: 10.1103/PhysRevD.95.024033
Preprint: arXiv:1410.8607v3 [gr-qc]
Cited on page 16

[40] Shibata M: Deriving formulations for numerical computation of binary neutron stars in quasicircular orbits; *Physical Review D (Volume 70, Issue 4)*, American Physical Society (2004).
DOI: 10.1103/PhysRevD.70.044044
Erattum in Volume 70, Issue 12, DOI: 10.1103/PhysRevD.70.129901
Preprint: arXiv:gr-qc/0407036v1
Cited on page 32

[41] Sperhake U: Binary black-hole evolutions of excision and puncture data; *Physical Review D (Volume 76, Issue 10)*, American Physical Society (2007).
DOI: 10.1103/PhysRevD.76.104015
Preprint: arXiv:gr-qc/0606079v2
Cited on page 15

[42] Strauss WA: Partial Differential Equations: An Introduction - Second Edition, John Wiley & Sons (2008).
ISBN: 978-0470-05456-7
Cited on page 48

[43] Thornburg J: Coordinates and boundary conditions for the general relativistic initial data problem; *Classical and Quantum Gravity (Volume 4 ,Number 5)*, Institute of Physics Publishing (1987).
DOI: 10.1088/0264-9381/4/5/013
Also as thesis: open.library.ubc.ca/cIRcle/collections/ubctheses/831/items/1.0085797
Cited on page 13

[44] Valiente Kroon JA: Nonexistence of Conformally Flat Slices in Kerr and Other Stationary Spacetimes; *Physical Review Letters (Volume 92, Issue 4)*, American Physical Society (2004).
DOI: 10.1103/PhysRevLett.92.041101
Preprint: arXiv:gr-qc/0310048v1
Cited on page 32

[45] Valiente Kroon JA: Asymptotic expansions of the Cotton-York tensor on slices of stationary spacetimes; *Classical and Quantum Gravity (Volume 21, Number 13)*, Institute of Physics Publishing (2004).
DOI: 10.1088/0264-9381/21/13/009
Preprint: arXiv:gr-qc/0402033v2
Cited on page 32

[46] Wald RM: General Relativity, The University of Chicago Press (1984).
ISBN: 0-226-87033-2
Cited on pages 5, 10

[47] Waxenegger G et al: Existence and uniqueness of Bowen-York trumpets; *Classical and Quantum Gravity (Volume 28, Number 24)*, Institute of Physics Publishing (2011).
DOI: 10.1088/0264-9381/28/24/245002
Preprint: arXiv:1107.3083v2 [gr-qc]
Cited on page 19, 34

[48] Weinberg S: Gravitation and Cosmology: Principles and applications of the General Theory of Relativity, John Wiley & Sons (1972).
ISBN: 0-471-92567-5
Cited on pages 5

[49] York JW: Kinematics and dynamics of general relativity; *Smarr LL editor, Sources of gravitational radiation (pages 83 126)*, Cambridge University Press (1979).
Cited on page 5, 8

[50] York JW: Conformal 'Thin-Sandwich' Data for the Initial-Value Problem of General Relativity; *Physical Review Letters (Volume 82, Issue 7)*, American Physical Society (1999).
DOI: 10.1103/PhysRevLett.82.1350
Preprint: arXiv:gr-qc/9810051v2
Cited on page 10

[51] Zlochower Y et al: Evolutions of nearly maximally spinning black hole binaries using the moving puncture approach; *Physical Review D (Volume 96, Issue 4)*, American Physical Society (2017).
DOI: 10.1103/PhysRevD.96.044002
Preprint: arXiv:1706.01980v2 [gr-qc]
Cited on page 16

Summary

This thesis is structured in two parts. In part 1 we summarise the necessary theoretical background and the numerical tools in order to conduct the research in part 2. In chapter 2 we summarise the $3+1$ approach to numerical relativity, with a focus on the initial data formalism in the weighted transverse and conformal thin-sandwich decompositions. We then move on to discuss initial data for black hole simulations in chapter 3, where we focus on the moving puncture approach. We note that the standard gauge evolution equations force the initial numerical wormhole slices to evolve into trumpet slices, which suggests the construction of a priori trumpet initial data. We summarise the literature on trumpet research, with a focus on maximal Schwarzschild trumpet initial data in its analytical form. In chapter 4 we provide the necessary numerical tools and techniques, which we use in part 2 to solve the constraint equations numerically. We focus on finite difference methods in connection with the Thomas algorithm and successive over-relaxation to solve boundary value problems in one and two variables.

Part 2 contains the novel research of this thesis. In chapter 5 we discuss Kerr in quasi-isotropic coordinates and point out that it represents a maximal trumpet foliation for extreme Kerr, however a wormhole foliation for slow Kerr. We lay out our approach to numerically derive maximal Kerr trumpet initial data. The approach is based on the proposition that two nontrivial impositions on the constraints suffice to construct the data numerically. We propose that these relations can be generalised from Schwarzschild and extreme Kerr to slow Kerr. The main motivation for this stems from the observation that the square of the extrinsic curvature for Bowen-York shows the same behaviour as for Kerr for small radii, and Bowen-York trumpets have been constructed successfully.

Our main results are then presented in chapters 6 and 7 in which we test our approach for the special cases of zero and maximal spin, ie for Schwarzschild and extreme Kerr. We succeed with Schwarzschild and present the first ever purely numerical derivation of maximal Schwarzschild trumpet initial data in the weighted transverse decomposition – our first main result. Because of the complexity of the problem for extreme Kerr, we proceed in steps and start out by using more information of the analytical solution to treat the constraints separately. For instance, we provide the conformal metric to the Hamiltonian and momentum constraints, and solve them successfully for the trumpet solution – our second main result. Finally we elaborate on how to relax the assumptions. In particular, we introduce an additional equation which we can solve successfully for the function which describes the deviation of the conformal metric from being flat – our third main result.